Controls on reflux dolomitisation of epeiric-scale ramps: insights from reactive transport simulations of the Mississippian Madison Formation (Montana and Wyoming)

Tatyana Gabellone [a*], Fiona Whitaker [a], David Katz [b], Graham Griffiths [a], Mark Sonnenfeld [b]

[a] School of Earth Sciences, University of Bristol, Wills Memorial Building, Queen's Road, Bristol, BS8 1RJ, UK (tatyana.gabellone@bristol.ac.uk; Fiona.whitaker@bristol.ac.uk, graham.griffiths@yahoo.co.uk)

[b] Whiting Petroleum Corporation, 1700 Broadway, Suite 2300, Denver, CO 80290-2300, USA (David.katz@whiting.com; MarkS@whiting.com)

*corresponding author

Abstract

Prediction of the geometry and petrophysical properties of dolomite geobodies depends on understanding both the hydrological system supplying reactive fluids and the chemistry of these fluids. However, patterns are complicated by the non-linear response of the diagenetic system to depositional texture, which controls both fluid flux *via* permeability architecture and reaction rate *via* effective surface area. This study explores interactions between extrinsic controls (spatial distribution of brine composition and temperature) and intrinsic controls (permeability and reactivity) using local and regional scale reactive transport models of sequential episodes of brine reflux that resulted in partial dolomitisation of the Mississippian Madison ramp.

Inter-well scale models show preferential early dolomitisation of fine grained, more reactive beds. Pervasive dolomitisation can occur most readily beneath the brine pool where flow is perpendicular to bedding, and is most rapid at high brine fluxes. Down-dip of the brine pool,

bedding-parallel flow is focused in relatively permeable coarse grained beds, providing reactants for strongly preferential alteration of intervening more reactive fine grained beds. In contrast, thicker sequences of fine grained beds dolomitise more slowly, limited by the rate of supply of magnesium. Regional-scale models, with injection of brines of increasing salinity towards the ramp interior, reproduce the observed pattern of dolomitisation. However, more realistic simulations in which reflux is driven by lateral density contrasts, generate flow rates orders of magnitude too low for significant dolomitisation. Simulations suggest pervasive dolomitisation of epeiric-scale ramps by a platform-wide reflux circulation, as often invoked, is not feasible. Rather, dolomitisation of such extensive systems critically requires local-scale flow systems, such as may result from topographically-controlled variations in restriction of platform-top seawater circulation.

Keywords

Reactive transport modeling, Madison Formation, reflux, dolomitisation, epeiric ramp, brine pools

1. Introduction

Dolomite formed by replacement of calcite can be mimetic, but in many cases fundamentally modifies the geometry of the pore network (Wardlaw, 1976; Lucia, 1995; Woody et al., 1996). Mud-dominated carbonates can be replaced by coarser sucrosic dolomite crystals with a resulting increase in pore size and also permeability up to three orders of magnitude (Lucia, 1995). Thus defining the geometry and characteristic of dolomite geobodies is important in assessing the distribution of reservoir quality. The chemical composition and flux of Mg-rich diagenetic fluids are key controls and vary with

the hydrological system driving dolomitisation (Morrow, 1982; Land, 1985; Warren, 2000; Machel, 2004).

In many important conventional carbonate reservoirs hydrocarbons are hosted in dolomites associated with reflux of platform-top evaporative brines (Sun, 1995). Within these systems primary porosity is commonly occluded by dolomite cement proximal to the brine source, whilst higher porosity and permeability are expected in more distal parts of the flow system where the brines are less dolomite-supersaturated (Lucia and Major, 1994; Saller and Henderson, 1998; Wahlman, 2010). However, such simple conceptual models predicting dolomite distribution and its effect on reservoir quality ignore both dependence on depositional texture and feedbacks during diagenesis, both of which have positive and negative influence on reservoir properties. Spatial variations in depositional texture control both fluid flux *via* permeability architecture and reactivity *via* the effective reactive surface area. Dolomitisation and associated diagenetic reactions modify the permeability, altering the distribution of fluid flux, and also modify reactivity, resulting in systematic changes in the distribution of water-rock interaction over time irrespective of changes in boundary conditions such as climate and relative sea-level.

Numerical simulations coupling fluid flow and diagenetic reactions have provided new insights into dolomitisation and associated diagenetic modifications. Small-scale one-dimensional reactive transport model (RTM) simulations of shallow reflux systems (Gabellone and Whitaker, 2016), for example, evaluated the sensitivity of dolomitisation to a range of extrinsic and intrinsic factors, suggesting a major control by brine composition, effective surface area of precursor sediments and temperature. Only in systems where fluid flux is very low do reactions become limited by supply of reactants rather than reaction

rate. Two-dimensional RTM simulations have also been used to investigate reflux dolomitisation, and specifically the spatial and temporal distribution of dolomite bodies and associated porosity modifications at a range of scales in generic carbonate platforms (Jones and Xiao, 2005; Al-Helal et al., 2012a). At the inter-well scale three-dimensional RTM simulations explored the effect of permeability and spatial distribution of platform-top brines (Xiao et al., 2013), showing that reflux associated with local brine ponds has the potential to generate complex distributions of dolomite with 'finger' orientations that reflect multi directional fluid flow with respect to depositional dip and strike.

These 2D and 3D models are capable to replicate processes observed in natural systems, and predict diagenetic patterns which in some cases differ from those of simple conceptual models. The introduction of even very simple horizontal layering of sediment texture or vertical fracturing produces spatially complex diagenetic patterns (Whitaker and Xiao, 2010; Al-Helal et al., 2012a). Jones and Xiao (2005) introduced a randomly distributed heterogeneous initial permeability which resulted in pronounced perturbations in the geometry of the simulated dolomite front (dolomite fingers). However, none of these previous studies considered the links between platform geometry and distribution of depositional facies. In natural systems, sequence stratigraphy exerts a strong systematic control on depositional texture. Previous RTM simulations (Gabellone and Whitaker, 2016) suggest that depositional texture should affect the pattern of dolomitisation through the combined control of fluid flux and effective reactive surface area. Resulting feedbacks are likely quite complex and their operation in carbonate systems with systematic spatial variations in the distribution of depositional facies are difficult to predict from first principles.

RTM simulations constrained by case studies provide an important advance on simple generic simulations, allowing both the use of a more realistic spatial facies distribution and the possibility to compare the model results with observations from real fields. Garcia-Fresca et al. (2009) simulated the impact of successive episodes of reflux during accumulation of a column of sediments to explain vertical variations in dolomite abundance and relationships to discontinuity surfaces in the Albian Glen Rose Formation in central Texas. In more recent 2D simulations Lu and Cantrell (2016) suggested that the lateral migration of an evaporative pond over time following deposition of the Jurassic Arab-D reservoir in the Ghawar field could explain the occurrence of non-stratigraphic (non-stratabound) dolomite bodies. Here we combine these two concepts, to investigate the diagenetic overprinting resulting from the interaction of syndepositional dolomitisation during deposition of an extensive prograding ramp with lateral and vertical facies contrasts, and changes in the position, extent and degree of evaporation in the brine pool developed at successive sequence boundaries.

We present numerical exploration of dolomitisation of the Mississippian Madison Formation ramp, which extended 700 km from the transcontinental arch in SE Wyoming into the Central Montana Trough. Previous detailed studies characterised the partially dolomitised ramp system and provided important constraints to help unravel key controls on reflux flow and resultant diagenesis (Elrick and Read, 1991; Sonnenfeld, 1996a and b; Smith et al., 2004; Buoniconti, 2008; Katz, 2008). Geochemical and fluid inclusion data from finely to medium crystalline dolomites of the mid-to-upper ramp indicate dolomitisation by Mississippian marine-derived fluids characterized by increasingly high salinity and alkalinity landwards (Katz, 2008). RTMs at the inter-well scale within an individual bed of the Madison Formation

explored lateral heterogeneities in porosity developed during early dolomitisation, which were interpreted to be the result of geochemical self-organisation (Budd and Park, 2011).

In this study, RTM simulations at the outcrop (inter-well) and regional scales are used to explore operation of and interaction between intrinsic facies-dependent controls and extrinsic factors such as spatial distribution and composition of brines and temperature, during sequential episodes of brine reflux during deposition of three 3rd-order cycles. Specifically we aim to address the following questions:

Can large scale reflux be driven by laterally extensive brine pools developed over epeiric platforms or broad ramps such as the Madison?

Does pervasive dolomitisation of such systems require overprinting by sequential reflux episodes generated during progradation of the ramp system?

Is dolomitisation always favoured in fine grained highly reactive sediments, or can also less reactive but more permeable coarse grained sediments be preferentially dolomitised in systems where reaction rates are limited by fluid flux?

2. Geological setting

The Madison Formation comprises an epeiric carbonate ramp deposited in water depths of 0->40 m in the Early Mississippian when the north-western part of modern North America was some 0-10° north of the paleoequator (Fig. 1). The ramp prograded north-west from the Transcontinental Arch and was bounded to the west by the deeper water Antler Foredeep, to the north by the Central Montana Trough and to the north-east by the Williston Basin (Gutschick and Sandberg, 1983; Sonnenfeld, 1996b). The Madison varies in thickness from *ca*. 15 m at Hartville Canyon in Wyoming to *ca.* 330 m at Livingstone in

Montana (Fig. 1; Sonnenfeld, 1996b). These carbonates were deposited unconformably, directly overlying the Precambrian basement in the up-dip area, and extending over the Cambrian Gallatin Formations and Ordovician Bighorn Dolomite to the south-east and the Devonian Jefferson and Three Forks Formations in the downdip sections to the north-west (Fig. 2A).

The Early Mississippian was a period of calcitic sea (greenhouse condition), characterised by low amplitude (<10 m) high frequency sea-level cycles superimposed on low frequency 3rd-order cycles (duration up to 6 My) with amplitudes from a few tens of meters up to *ca.* 120 m (Haq and Schutter, 2008). According to the sequence stratigraphic framework of Sonnenfeld (1996b; Fig. 2A), the Madison evolved from a ramp (Sequences I and II) to a flat-topped rimmed shelf (Sequence III). Each of these 3rd-order sequences represents about 2 My and comprises a series of higher frequency cycles (0.1-1 My).

Sequences I to III were deposited in an arid climate and large parts of the platform were affected by early marine derived dolomitisation, with evidence for brine reflux (associated with evaporite deposition), as well much more localised hydrothermal calcite cementation and dolomitisation, with associated minor-to-trace amounts of both replacive and cementing quartz and fluorite minerals (Sonnenfeld, 1996b; Moore, 2001; Katz et al., 2006). In contrast the overlying Sequences IV to VI (not shown), which lack dolomite, were deposited under a more humid climate (Sonnenfeld, 1996b). Within Sequences I to III dolomitisation is pervasive in the inner ramp and is not fabric selective (Fig. 2B), whereas in the mid-ramp mud-dominated carbonate sediments are preferentially dolomitised and grainier units are partially dolomitised to limestone (Katz, 2008). There is no significant dolomitisation at the margin or basin (Fig. 2B). Two regional solution collapse breccias were

recognised at the base of Sequences III and IV. These breccias formed by the dissolution of massive evaporite beds and the collapse of overlying strata (Sonnenfeld, 1996b; Smith et al., 2004; Katz et al., 2006, Zahm et al., 2015), and can be correlated laterally with 30 m thick undissolved evaporites (anhydrite) present in the subsurface of the Williston basin (Middleton, 1961; Roberts, 1966).

3. Methods

3.1 Approaches to numerical simulations

Reactive transport modelling (RTM) is a numerical tool allowing the coupling of multiphase fluid and heat flow, solute transport and chemical reactions in heterogeneous porous media. Multiple episodes of brine reflux dolomitisation were simulated in the Madison ramp using the RTM code TOUGHREACT (Xu et al., 2004). The code allows the tracking of fluid flow and chemistry, but also mineral precipitation and dissolution and porosity evolution at a range of scales.

The geochemical composition of the brines used as inputs to the TOUGHREACT simulations was derived by simulating the effect of evaporation of Mississippian seawater using PHREEQC (Parkhurst and Appelo, 1999). This computer program is based on an ion-association aqueous model and has capabilities to perform speciation, batch-reaction, inverse modelling and one-dimensional reactive transport. We use the Pitzer specific-ion interaction model in both PHREEQC and TOUGHREACT simulations as this is more reliable for high ionic strength than the Debye-Hückel approach. In simulations of brine reflux, the Pitzer model has been shown to yield higher rates of dolomitisation and gypsum precipitation (Al-Helal et al., 2012b), and is employed by some of the most recent RTM

studies of dolomitisation (Al-Helal et al., 2012b; Gabellone and Whitaker, 2016). The thermodynamic data were taken from the EQ3/6 geochemical database (Wolery, 1992) with corrections (see Gabellone and Whitaker, 2016 and references therein).

3.2 Rock properties

All our TOUGHREACT simulations include vertical variations in facies. Facies differences influence the reduction in porosity and permeability with depth due to compaction, and also the effective reactive surface area (RSA). Regional scale models also comprise lateral variations in facies. The models were populated with 10 different rock types (table 1; Fig. 3) which were derived from the 16 facies described by Sonnenfeld (1996b) by merging those with similar texture. Each rock type is characterised by a different fine fraction (F_f), defined as the fraction of granular component <63 µm. The depositional porosity (ϑ_i in %) for each rock type was calculated based on the percent of fine fraction (f_f) using empirical relationships from modern sediments (following the approach developed by Smart et al., 2005, based on data from Enos and Sawatsky, 1981, and Bennett et al., 1990). For sediments of >15% fine fraction percent porosity is:

$$\vartheta_i = 20.02 * f_f^{\,0.306} \qquad \text{(equation 1)}$$

whilst at lower fine fraction porosity is set at 45%. Each rock type was decompacted to generate three sets of depth dependent porosity (ϑ_z) for times corresponding to the end of deposition of Sequences I, II and III, based on fine fraction (Smart et al. 2005, fit to data from Goldhammer, 1997):

$$\vartheta_z = [\, 45.0 \exp^{-z/5500} \,] - [\, G_p . ln\,(z) - I_p \,] \qquad \text{(equation 2)}$$

Porosity declines exponentially with depth (z in m), and the gradient (G_p) and intercept (I_p) are dependent on depositional porosity and thus texture:

$$G_p = 0.0951\vartheta_i - 4.245 \quad \text{(equation 3)}$$

$$I_p = 0.629\vartheta_i - 27.84 \quad \text{(equation 4)}$$

We estimate matrix horizontal permeability (K_h in mD) from porosity and fine fraction following the approach of Lucia (1995, 2007) that identifies a continuum of rock fabrics and associated poro-perm transforms (Smart et al., 2005):

$$K_h = (1.14e\text{-}3 * F_f) * [\vartheta_z^{\wedge((-1.871 * Log10(Ff)) + 2.513)}] \quad \text{(equation 5)}$$

The vertical permeability (K_v) was calculated from k_h based on a permeability anisotropy (K_h/K_v) assigned to each rock type (table 1). The sensitivity to a higher anisotropy (one and two orders of magnitude) was explored for one set of simulations (Simulation 6, see paragraph 3.3).

Changes in porosity during the simulation are calculated from changes in mineral volume fractions, reflecting the dissolution and precipitation of minerals of different densities. The evolution of permeability with porosity is modelled using a Carman-Kozeny relationship, consistent with previous RTMs of dolomitisation (Whitaker and Xiao, 2010; Al-Helal et al., 2012a):

$$K_{ht} = K_h \frac{(1-\theta_z)^2}{(1-\theta_{zt})^2} \left(\frac{\theta_{zt}}{\theta_z}\right)^3 \quad \text{(equation 6)}$$

where K_h and θ_z are the initial permeability and porosity, respectively, and K_{ht} and θ_{zt} are permeability and porosity at time *t*.

In simulations where the flow rate is externally specified (1D models of Simulation 1, see paragraph 3.3), there is no feedback between diagenetic changes and reactions, as flux is constant through time. In contrast, in the 2D models where injection rate is specified (Simulations 2 and 3) patterns of fluid flux, and thus reactions, are sensitive to alteration during prior time steps. This is also true where flow is driven by density differences (Simulations 4, 5 and 6), though in addition in these simulations diagenetic changes can alter the total fluid flux, with reactions that increase porosity giving rise to higher flux due to the calculated increase in permeability.

TOUGHREACT uses RSA to initialise nucleation of kinetic minerals (see paragraph 3.4). To investigate possible control on sediment reactivity by sediment texture, we used the fraction of fines in combination with geometric calculations to estimate the RSA for each rock type (table 1; Fig. 3D). Resulting RSA varies from 7.2 m^2/kg to 50 m^2/kg, representing rhombic crystals with diameter from 360 and 50 μm. RSA modifications due to diagenetic changes in texture during dolomitisation are currently not included in our simulations. Given the uncertainty in RSA evaluation, we replicated one set of simulations (Simulation 6, see paragraph 3.3) using one and two orders of magnitude higher RSA for each rock type.

3.3 Hydrological systems and simulations

Six different sets of simulations were performed and are summarised in table 2. Simulation 1 is a set of 1D RTMs of a single 3rd-order sequence (Sequence I) based on lithologies described at the Sheep Mountain outcrop (Sonnenfeld, 1996b; Fig. 4). The thickness of the section after decompaction is 45 m. The model consists of 130 cells with variable thickness from 0.19 m to 2.04 m reflecting the thickness of the depositional layers. Given the shallow depth of the system simulated we do not expect significant geothermal heating. The model

is thus isothermal, with a temperature of 35 °C determined by the bank top temperature, based on global paleo-ocean surface water temperature reconstructions (Markello et al., 2007). The model is initially saturated with normal Mississippian seawater of 35 ‰ salinity (g salt/kg seawater; see section 3.4 for details on seawater and brine chemistry). We simulated reflux by injecting at a constant rate a 110 ‰ salinity brine (3x seawater) at the top of the column, with discharge from the base. Reflux rate will be determined by the balance between the gradient in effective head and the permeability along the flow path. We explored four different injection rates of 1, 0.1, 0.01 and 0.001 m/yr, and ran each simulation for 1 Myr. This model design assumes that the sediments were located beneath the brine pool, where generic simulations suggest that flow will be mainly vertical (Al-Helal et al., 2012a).

Although the sediments exposed at Sheep Mountain were overlain by the brine pool developed after deposition of Sequence III (Figs 2A and 6), at the end of Sequence I they were downdip of the brine pool. We therefore also developed a 2D simulation whereby the section was affected solely by lateral flow of brines (Simulation 2). In this model the vertical variations in facies within the decompacted Sequence I were extended laterally for 3000 m. Field mapping suggests minimal variation in depositional facies along the length of the outcrop (Sonnenfeld, 1996b; Katz, 2008). This grid has 19,500 cells, each 20 m wide and varying in thickness from 0.19 m to 2.04 m. Rock types are identical to those in the 1D model (Fig. 4), and simulations remain isothermal, at 35 °C. The same 110 ‰ salinity brine was injected at a constant rate from the right side of the model, whereas the left side represented an open (discharge) boundary. The distribution of lagoonal facies (Sonnenfeld, 1996b; Fig. 2A) suggests that the brine pool developed at the end of Sequence I likely

extended some 180 km parallel to the dip. Assuming vertical recharge at 0.01 m/yr from this brine pool, we calculated a total flux of 38.9 $m^3/m^2/yr$ across the right boundary of the 2D Sheep Mountain model. This flux assumes no brine discharge into updip areas of the ramp, and thus we compare this simulation with one with a flux based on recharge at 0.001 m/yr.

Four different sets of 2D regional-scale simulations were performed. Simulation 3 is an isothermal model of Sequence I in which brines are injected across the inner 180 km of the ramp at constant fluid flux of 0.001 m/yr (Fig. 5A). This is compared with non-isothermal simulations where the brine inflow rate is determined by the density distribution of fluids within the ramp system relative to those at the top boundary of the model (Simulations 4, 5 and 6; Fig. 5B). In these last three sets of simulations we model stepwise accumulation and flow through Sequences I, II and III with changing distribution of brines of the platform top. Finally a sensitivity analysis based on Simulation 6 is performed for Sequence I.

The grids for these models comprise up to 28,500 active cells, each 1178 m in width (except those in the furthest 125 km of the basin where cells are 25 km in width) and varying in height between a minimum of 0.15 m in the interior to a maximum of 5.7 m in the Central Montana Trough. Sequence I comprises 8,000 cells, Sequence II adds a further 7,500 cells, and Sequence III adds 13,000 cells. The relatively low permeability rocks underlying the Madison are specified at coarser resolution, and account for an additional 1,500 cells which range from 20 to 93.6 m thick. Each full simulation of Sequences I to III requires in excess of one month run time on a Linux supercomputer node with 16 cores running at 3.66 Ghz and 192 GB RAM.

Regional-scale models use the sequence stratigraphic framework of Sonnenfeld (1996b) which describes a 600 km long SE-NW section from the Hartville Canyon to Livingstone (Fig.

2A), constructed by integrating outcrop measured sections with cores from subsurface reservoirs. The section was extended 100 km into the Montana Trough, which was 500 m deep at the start of deposition of Sequence I but shallowed to <50 m at the end of Sequence III. The sedimentary architecture and the rock properties in this additional part of the section were based on facies distribution of Buoniconti (2008) which extends the cross-section from Livingston to Monarch. Only the first three Madison sequences are simulated, on the basis that dolomitisation does not affect Sequences IV to VI. The rocks underlying the Madison were also included in the model domain, assuming a homogeneous low porosity and isotropic low permeability (10% and 10^{-18} m^2 respectively). Water depth, used to calculate pressure across the top boundary, was specified using interpreted minimum and maximum water depths for different facies types/assemblages at the top of each of the three sequences (Katz, 2008). The absolute depth of each facies-bounding time line was then adjusted for decompaction (see section 3.2).

Left and right boundaries of all the regional scale models are no-flow (Fig. 5). The lower boundary is closed to flow and solute transport, but in non-isothermal simulations (Simulations 4, 5 and 6; Fig. 5B) is open to heat transport with a basal heat flux typical of passive-margin settings (65 mW/m^2). The top boundary is open, allowing the recharge or discharge of fluids. In non-isothermal simulations the temperature on the platform top (water depths < 2 m) is specified as 35 °C, decreasing within the basin at 5 °C/100 m depth (after oxygen isotopes measurements on Early Mississippian brachiopods from Stanton et al., 2002).

The model is initially saturated with Mississippian seawater. Brines are specified along the top boundary of each sequence in the inner part of the ramp (right of the model). The width

of the brine pool in Simulations 4, 5 and 6 increases with time reflecting the progradation of the ramp, from 180 km, to 234 km and 580 km for Sequences I, II and III respectively. These widths are constrained by the reported locations of lagoonal facies for Sequence I and evaporite solution collapse breccias for Sequences II and III (Sonnenfeld, 1996b).

The assumed timescale for reflux in each sequence is 1 Myr, representing half the estimated total duration of the 3rd-order cycles which deposited the sequences (Katz, 2008). Modelling stepwise evolution of the three sequences involves RTM of decompacted Sequence I. This is followed by addition of decompacted Sequence II on top of the diagenetically altered Sequence I and compaction of Sequence I reflecting shallow burial. RTM of the combined Sequences I and II is performed. Finally Sequence III is added on top of Sequence II and the workflow is repeated. The geometry of these models, the distribution of sediment permeability and RSA, and the brine distribution on the ramp top is shown in Figure 6.

All regional scale simulations assume a very broad (180-580 km wide) zone of brine generation extending across the ramp from the right boundary. In Simulation 4 we specify brine salinity increasing linearly towards the ramp interior (see section 3.4; Fig. 5C). However, spatial and temporal variations in brine salinity would likely result from local variations in ramp geomorphology related to sub regional subsidence-related tectonism (Buoniconti, 2008) across such an extensive ramp. Simulation 5 uses multiple brine pools at the top of each sequence. The number of brine pools, their width and spacing were assigned arbitrarily, but the total width of the brine sourcing area for each sequence is constrained by the locations of lagoonal facies and evaporite solution collapse breccias. Five brine pools were specified in each sequence: in Sequence I they are around 20 km wide and spaced 20 km apart; in Sequence II the width and spacing of the pools is around 25 km, whilst in

Sequence III they have a width of 84 km and a spacing of 40 km. The final set of simulations (Simulation 6) assumes for each sequence a broad brine pool (from 180 in Sequence I to 580 km wide in Sequence III) in which brine salinity varies in a random manner about the overall linear gradient used in Simulation 4 (Fig. 5D).

3.4 Brine composition, mineralogy and kinetic parameters

The chemistry of the brines which formed the Madison dolomites is not well constrained. Based on oxygen isotopes measurements of bulk samples from calcitic and dolomitic mudstones to grainstones, Katz (2008) suggested only marginal increase in salinity across the Madison ramp from normal seawater (35 ‰) in the outer ramp up to 41-44 ‰ (mesosaline brines) in the updip locations where there are more restricted conditions. However, fluid inclusions data for fine-crystalline fabric selective dolomites indicate very much higher salinities, up to 21.9 wt % eq. NaCl (a salinity of 219 ‰). Moreover the presence of relicts of gypsum in the dolomitised carbonates (Katz, 2008) is also indicative of brines with salinity of 140-250 ‰ (Warren, 1999). It is reasonable to assume that evaporative brines generated along the Madison ramp were at least gypsum-saturated and were increasingly more concentrated towards the updip locations.

Given this uncertainty, a number of simulations were performed with differing brine pool salinities. In the 1D and 2D inter-well scale models (Simulations 1 and 2) reflux was simulated using a single 110 ‰ salinity brine. In the 2D basinal scale models with brine injection (Simulation 3) and with density-driven flow (Simulation 4), we specified a range of brines progressively more concentrated towards the ramp interior (increasing by 0.44 ‰/km) from normal seawater (35 ‰) up to maxima of 110 ‰ and 142 ‰ in Sequences I and II, respectively (Fig. 5C). In Sequence III, the salinity of the brine increases to a maximum

of 142 ‰ over 328 km and thereafter remains constant in the innermost part of the platform (Fig. 5C).

In Simulation 5, in each of the three 3rd-order sequences, each of the five brine pools has a different brine salinity, reflecting progressive concentration towards the inner ramp, and is separated by an area of normal marine seawater (35 ‰). In Sequence I brine pool salinity varies from 89 to 110 ‰, whilst in Sequences II and III there are brines of 121 to 142 ‰ salinity. For the final set of simulations (Simulation 6) random variations in salinity were superimposed on the linear trends of Simulation 4 (Fig. 5C). Using a range of ±70 ‰ but capping the minimum salinity at 35 ‰, this yielded values ranging over 35-163, 35-195, and 35-211 ‰ salinity for Sequences I, II and III respectively.

Whilst fluid density is a continuous function of salinity, a more limited number of brine chemistries are specified (15 in Sequence I and 21 in both Sequences II and III). The composition of these brines was derived by simulating the effect of evaporation of Mississippian seawater, with incremental increases in salinity of 5 ‰. The seawater composition (Mg/Ca molar ratio of 2.3) was taken from Demicco et al. (2005), who used an inverse model that considers variable rates of seawater cycling through axial portions of mid-ocean ridges. Paleo-pH and atmospheric pCO_2 were taken from Zeebe (2012), and were used to calculate carbonate alkalinity using CO2SYS (Pierrot at el., 2006) with dissociation constants from Mehrbach et al. (1973) refit by Dickson and Millero (1987). The saturation state of each brine with respect to carbonates and evaporite minerals is expressed by the saturation index (SI), which is the log of the ratio between the ion activity product and the equilibrium constant.

Geochemical calculations in TOUGHREACT include 9 primary (H_2O, H^+, Ca^{2+}, Mg^{2+}, Na^+, K^+, HCO_3^-, SO_4^{2-} and Cl^-) and 11 secondary aqueous species ($CaCO_3(aq)$, $CaHCO_3^+$, $CaOH^+$, $CaSO_4(aq)$, $CO_2(aq)$, CO_3^{2-}, HSO_4^-, $MgCO_3(aq)$, $MgHCO_3^+$, $MgOH^+$ and OH^-). Initial mineralogy is specified as 99% calcite throughout the Madison, with 1% "seed" dolomite which provides nucleation sites for dolomitisation. The underlying basement is assigned as unreactive non-carbonate. We assume no primary evaporite minerals are present at the beginning of the simulation, but allow for the precipitation of diagenetic gypsum or anhydrite. Dolomite precipitation is much slower than dissolution or precipitation of calcite, gypsum and anhydrite. We thus model these three as thermodynamic minerals, precipitating or dissolving to drive any solution to equilibrium within one timestep. In contrast, dolomite precipitation is modelled as a kinetic process using the rate law of Arvidson and Mackenzie (1999):

$$r_{\mathrm{dol}} = A_{\mathrm{s}} A e^{-\left(\frac{E_{\mathrm{a}}}{RT}\right)} \left(1 - \frac{Q}{K_{\mathrm{eq}}}\right)^{2.26} \qquad \text{(equation 7)}$$

where r_{dol} is the reaction rate of dolomite; A_{s} is the specific reactive surface area; Q is the activity quotient, and K_{eq} is the equilibrium constant for dolomite; A, the pre-exponential factor, is 11.2 mol/cm^2/s; E_a, the activation energy, is 1.335 x 10^5 J/mol; R is the universal gas constant; T is the temperature (in Kelvin); and 2.26 is the reaction order.**4. Results**

4.1 Inter-well scale 1D and 2D models of the Sheep Mountain outcrop

Vertical reflux of 110 ‰ Mississippian brine (SI_{dol}= 4.0) at 35 °C through a 45 m thick 1D column representing the uncompacted stratigraphy described at Sheep Mountain (Simulation 1) drives dolomitisation which is focused initially in more reactive beds of finer grained sediments. Figure 7 shows the facies control on the increase in the amount of

dolomite at six time steps between 50 kyr and 1 Myr. Simulations with fluid flux ranging from 0.001 to 1 m/yr show that reaction rates are directly dependent upon the rate of supply of diagenetic reactants and removal of products. By definition in 1D simulations fluid flux is identical in all cells, though residence times of fluids scales directly with porosity, contributing to higher reaction rates in finer grained sediments. For the fastest flow rate, calcite is completely replaced by dolomite within 200 kyr in the more reactive (RSA> 20 m^2/kg) mudstones/wackestones of the Restricted Lagoon (RL), wackestones of the Middle Ramp (MID) and packstones/grainstones of the Lower Shoreface (LSF). The micropeloidal grainstones of the Back Shoal Lagoon (BSL) with an RSA of 18.5 m^2/kg also reach 90 % dolomite. In contrast, the less reactive packstones/grainstones of the Middle Upper Shoreface (MUS) and grainstones of the Restricted Upper Shoreface (RUS) remain largely calcitic (7-21 % dolomite) after 200 kyr, complete dolomitisation requiring continuous flux of brines over up to 500 kyr and 1Myr in the MUS and RUS respectively. High rates of reflux (1 m/yr) ensure dolomitisation continues to depths of >40 m below the brine pool. However, at lower injection rates, longer residence time causes more rapid dolomitisation at shallow depth, depletion of Mg^{2+} in the percolating refluxing brine and a decrease in dolomitisation rate with depth below the brine source.

Replacement of calcite by dolomite (which generates porosity due to differences in mineral density) is accompanied by simultaneous precipitation of primary dolomite cements. Slow initial rates of replacement result in minor (<3%) net porosity reduction, for all but the slowest reflux rates (0.001 m/yr; Fig. 7F-M). As dolomite abundance increases (>50%), replacement rates accelerate and porosity is enhanced by up to 6% relative to the initial model. Following complete replacement of calcite, dolomite continues to form as primary

cement. In all simulations other than the very highest fluid fluxes, this dolomite precipitation ("overdolomitisation") and the consequent porosity decrease is limited to the upper 10 m of the column, preserving higher porosity in deeper sediments. At the lowest flux rates (<0.01 m/yr) Mg^{2+} supply is insufficient to drive significant dolomite cementation (Fig. 7I and M).

The effects of lateral flow of brine on dolomitisation at the inter-well scale were evaluated through 2D modelling of Sequence I at Sheep Mountain (Simulation 2). Flow of 110 ‰ brine parallel to the stratigraphy is focussed in the more permeable beds (Fig. 8B). By 200 kyr, flow rates within the RUS and MUS exceed 500 m/yr and 100 m/yr respectively, driven by reflux at 0.01 m/yr across a 180 km wide brine pool (Fig. 6A). Velocities are considerably lower (<20 m/yr) in the less permeable beds. The flow focused in these permeable beds provides reactants for strongly preferential alteration of adjacent more reactive fine grained beds. Thus after 200 kyr the modelled 2D section of Sheep Mountain shows alternation of completely dolomitised mudstones/wackestones and largely calcitic (5 to 22% dolomite) packstones/grainstones. Extracted 1D data displaying the temporal evolution of dolomitisation (Fig. 8C) show more rapid alteration of thin (<1-2 m) muddy beds independent of depth below the top of the sequence. Reduction of flow rate by an order of magnitude results in slower dolomitisation, so that even after 500 kyr the thick basal MID unit remains less than 14% dolomite (Fig. 8D). Both simulations show how alternation of more reactive and lower permeability beds with less reactive and more permeable carrier beds favours dolomitisation of the thin fine grained units in the upper part the sequence. In contrast, the 2D simulation shows how the lower fluid flux provides a significant limitation

to dolomitisation, despite the high reactivity of the much thicker wackestone (MID) unit which forms the basal 20 m of the sequence.

4.2 Regional scale 2D isothermal RTM of Sequence I with brine injection

The regional-scale distribution of reflux dolomitisation was initially simulated under isothermal conditions (35 °C) over 1 Myr (Simulation 3) by injection at a constant rate of 0.001 m/yr of 15 evaporative brines (from 35 to 110 ‰) increasing in salinity across the 180 km wide brine pool at the top of Sequence I (Fig. 9A-C, E and G). At this scale it is not possible to discriminate finer scale layering (<3 m) which controls the distribution of reactions in the inter-well scale simulations. Flow is predominantly vertical down through the shallow mudstones/wackestones of the upper RL, driven by strong lateral flow (up to 325 m/yr) in the underlying high permeability conduit given by grainstones of the RUS (Fig. 9C). In contrast, the lateral flow rates within the lower permeability mudstones/wackestones of the RL beneath this RUS unit are low (<1 m/yr). Most of the brines discharge within 180 km at the distal edge of the brine pool (Fig. 9E).

Dolomitisation is restricted to the area beneath the brine pool, whilst beyond the distal margin of the brine pool the Madison ramp remains mostly undolomitised (Fig. 9G). Vertical flow through the reactive RL underlying the brine pool gives rapid dolomitisation. The mudstones/wackestones of the RL at the base of Sequence I (from 0 to 110 km) are largely undolomitised due to the low fluid flux beneath the RUS conduit which acts as a thief zone protecting these reactive sediments from alteration by the refluxing brines. The localized reduction of permeability within this conduit, which marks the transition to MUS at *ca.* 110 km, is sufficient to drive downward flow of brines into the most distal part of the basal RL unit and through the LSF, and thence into the grainstones and packstones of the RUS and

MUS. Here again the system appears to be reaction rate rather than flux limited, with much of the less reactive RUS and MUS remaining only partially dolomitised (up to 18 %).

Only a minor amount of gypsum (< 4%) forms locally beneath the dolomite body in the innermost ramp (see Fig. A in the online supplemental material). Gypsum precipitation is driven by the reaction of the calcium released by replacement dolomitisation with the available sulphate in the brines. The change in porosity resulting from dolomitisation is calculated from the difference between the initial porosity, and the final porosity plus the volume fraction of gypsum (Fig. 10). The replacement of calcite by dolomite is accompanied by a porosity increase of up to 8%, with no overdolomitisation. Formation of the upper part of the dolomite body generates less porosity than dolomitisation of the RUS (Fig. 9B and G), which has a much lower initial porosity and thus a larger volume fraction of calcite available for dolomitisation.

4.3 Regional scale 2D non-isothermal RTM during stepwise deposition of Sequences I, II and III with density-driven fluid flow

In Simulation 4 flow is driven by the gradient in effective head caused by contrasts in fluid density across the top of the ramp. In addition, geothermal heat is input from the base of the model into units underlying the Madison. This results in very slow rates of geothermal convection of normal seawater in areas of the ramp beyond the distal edge of the brine pool. Given the limited thickness of the Sequence I carbonates, temperatures remain relatively low (<37 °C; see Fig. B in the online supplementary material) throughout the ramp. The spatial distribution of flow is similar to that developed in the model with brine injection, with lateral discharge focused in the high permeability RUS conduit beneath the brine pool (Fig. 9D). However, with density-driven flow the absolute flow velocities are some four

orders of magnitude lower. Low fluxes result in a poorly developed brine plume in Sequence I and no significant dolomitisation (Fig. 9F and H). After 1 Myr of simulation time, dolomite is limited to the upper 2 m of the mudstones/wackestones of the RL beneath the brine pool. Whilst maximum of 22 % dolomite occurs, over most of this shallow zone the abundance of dolomite is an order of magnitude lower.

Two further episodes of reflux from brine pools at the top of Sequences II and III, each sustained for 1 Myr, overprint the previously diagenetically altered sequences (Fig. 11). Dolomite formed during each episode acts as a seed for dolomitisation during subsequent periods of brine generation. With the accumulation of a thicker sequence temperatures increase (see Fig. B in the online supplementary material), but only reach a maximum of 42 °C at the bottom of the distal ramp (beyond 450 km). These factors might be expected to result in greater dolomite abundance in older sequences. However, simulations show most abundant dolomite near the top of Sequence III. As the ramp progrades, the width of the brine pool and salinity of brine both increase, resulting in higher hydraulic heads and more rapid (>1 order of magnitude) fluid flow. Flux is focused within the laterally extensive zone of relatively permeable RUS and MUS facies within Sequence II. These allow development of small-scale convection cells entraining seawater from the ramp top beyond the influence of refluxing brines during Sequence II, and also act as flow conduits for brines towards the distal edge of the brine pool in Sequence III. In contrast, brines sourced from the inner part of the brine pool permeate the subsurface of the platform interior during Sequence III times, but solute transport is dominated by diffusion rather than advection due to the lack of lateral head gradient in the inner 300 km of the ramp at this time.

Key characteristics of the inter-well scale models are honoured by this simulation, with fluid flux focused in more permeable units driving alteration in adjacent more reactive sediments. This results in a relatively greater abundance of dolomite in fine grained units, as observed in core and outcrop (Sonnenfeld, 1996b; Smith et al., 2004). However, even after diagenetic overprinting during deposition of three 3rd-order sequences over 3 Myr the predicted dolomite abundance remains very low (<10% over large areas, and only locally up to 100%). Whilst prior episodes of dolomitisation increase reaction rate over time, the lateral extension of the brine pool within Sequence III (over 580 km) actually serves to reduce the overall hydraulic gradient and flux limits reactions. Replacement dolomitisation is accompanied by precipitation of some diagenetic gypsum (up to 29 % after 3 Myr), which occur within areas of greater dolomitisation near the top surface of Sequence III (see Fig. A in the online supplementary material).

In Simulation 5 the single brine pool, which generates a relatively low hydraulic gradient, is replaced by five brine pools in each of the three sequences (Fig. 12A-D). In this model, absolute fluxes are one order of magnitude higher than in Simulation 4, with high effective head gradients develop at the edge of each pool driving discharge of brines. Higher fluxes still occur in the more permeable RUS and MUS, leading to more rapid dolomitisation. Thus, after 3 Myr, the limestones at the margins of each pool are almost completely replaced (>70 % dolomite), forming mostly vertically-oriented dolomite bodies. Basinward of the brine pools of Sequences I and II dolomitisation is only minor (<10 %) and affects primarily the most reactive, fine-grained rock types. Some gypsum (up to 33 %) precipitates beneath each vertical dolomite bodies (see Fig. A in the online supplementary material).

In Simulation 6 random variations in salinity superimposed on the regional salinity gradients represent the effect of a complex micro-topography on ramp-top circulation and resulting brine generation. Although absolute flow velocities are of the same order of magnitude than in Simulation 5 (with five brine pools; Fig. 12F), steeper local gradients in effective head enhance density-driven flow and thus dolomitisation, most notably in Sequences I and II, with initial preferential alteration of mud-dominated more reactive sediments (Fig. 12H). As a consequence of the greater rate of dolomite formation, and thus calcium release, precipitation of gypsum is also greater and affects larger areas, locally only reaching a maximum of 75 % (see Fig. A in the online supplementary material). With the overprinting of two or more episodes of dolomitisation affecting the carbonates of Sequences I and II, large areas of the inner ramp are completely altered.

Sensitivity to both anisotropy of permeability and effective reactive surface area is investigated for Simulation 6 using Sequence I only (Fig. 13). Increasing the RSA results in more complete dolomitisation of the RUS beneath the brine pool and dolomite extends to the base of the model within the RUS underlying the LSF. However the diagenetic increase in permeability in this RUS "thief zone", which is reflected in the higher overall reflux rate, means there is less dolomitisation of underlying RL limestones. Near the distal part of the brine pool increasing the RSA results in dolomite extending to the base of the carbonate, including the RUS unit in which dolomitisation was limited in the baseline simulation by the low RSA. Increasing the horizontal permeability leads to a significant increase in the flux of brines into the platform. Vertical tongues of dolomite extend into the lower RL unit from the base of the RUS, though the increase in dolomite fraction in more distal permeable

facies is still limited by their low reactivity. With both increased RSA and horizontal permeability, large areas of the ramp beneath the brine pool are totally dolomitised.

In all of these regional scale non-isothermal simulations (Simulations 4, 5 and 6) dolomitisation enhances porosity by up to 10% (not shown), whilst overdolomitisation does not take place.

5. Discussion

One-dimensional inter-well scale RTMs of brine reflux show that within individual fine-grained beds, dolomitisation rates are greatest at the top of the bed and decline with depth due to consumption of Mg^{2+}. With continued reflux, this alteration extends to grain-supported beds, with pervasive dolomitisation occurring initially at shallow depth but extending over the entire 45 m over a period of 0.5-1 Myr at all but the lowest specified flow rate. These results accord well with core and outcrop observations of pervasive dolomitised inner ramp areas irrespective of facies. These areas were inferred to have been most restricted and hosted brine pools at intervals corresponding to the top of Sequences I, II and III (Sonnenfeld, 1996b; Smith et al., 2004; Katz, 2008). Sediments underlying the brine pools are likely to have been affected by a significant component of vertical brine recharge, with an element of flux perpendicular to bedding. However, by definition a 1D model imposes an equal fluid flux through all units in the sequence. In doing so the model simulates neither the effect of reduced fluid flux which is likely through the lower permeability mud-supported units, nor the effect of feedbacks between permeability, flux of reactants and diagenetic alteration.

These limitations are largely overcome by the 2D models which show focusing of fluid flow through more permeable units. The inter-well scale models of Sequence I at Sheep Mountain that simulate brine flow parallel to bedding confirm preferential dolomitisation of the more reactive mudstone/wackestone beds is not dependent on fluids being forced vertically through the sediment column. Reactants are delivered to these more reactive mud-supported beds through adjacent more permeable but less reactive grainstones/packstones, which initially (by 200 kyr) remain mostly undolomitised. Dolomitisation proceeds at a faster rate in sequences where the thin fine-grained beds are interlayed with permeable coarser-grained beds, whereas in the more massive fine-grained beds dolomitisation is limited by the supply of magnesium. However the simulations suggest that despite low flow rates, dolomitisation of this massive lower unit is achieved whilst the grain-dominated units remain calcitic. An extended period of circulation is required (up to 1 Myr) before the 2D inter-well scale simulations show pervasive dolomitisation, based on inflow of either 0.01 or 0.001 m/yr across a 180 km wide brine pool at the top of Sequence I.

The Sheep Mountain outcrop is located in the mid-ramp (at a distance of ca. 150 km from the distal margin of the ramp system) and probably experienced lateral flow of brines during the deposition of Sequence I. Here the sequence shows fabric-selective dolomitisation of the mud-supported facies, with shoreface grainstones and packstones remaining calcitic (Sonnenfeld, 1996b; Smith et al., 2004; Katz, 2008).

Results from the 2D inter-well simulations of this study are consistent with previous RTMs using much thicker (50 m) horizontal units of either high permeability low reactive grainstones or low permeability high reactive mudstones set within a grain-dominated packstone matrix (Al-Helal et al., 2012a). The effect of high resolution alternations of

sediment texture such as modelled for Sheep Mountain are represented in this study by a high (10^3) permeability anisotropy. As for our simulations, at this much coarser resolution flow of brines is always focused within more permeable layers. However, the effect of these thick contrasting units on diagenesis is complex, with preferential dolomitisation of the more reactive but less permeable beds occurring only when the system is not flux-limited. A thick muddy unit can thus constrain flow completely to the overlying sediments. Other RTMs using higher-resolution layering of grain- and mud-dominated beds to echo the depositional sequence in the Arab-D formation of Ghawar suggest higher dolomite abundance in intermediate permeability and reactivity packstone layers, probably due to the combined effects of flow rate and sediments reactivity (Al-Helal, 2012; Lu and Cantrell, 2016).

The results of 1D and 2D models of Sheep Mountain agree with generic 1D simulations of brine reflux using brines derived from evaporation of Mississippian seawater in a homogeneous column of limestone (Gabellone and Whitaker, 2016). Both models show concurrent replacement of calcite by dolomite and dolomite cementation, with rates of both processes enhanced by fast flow rates. Porosity, initially enhanced by the mole-per-mole replacement of calcite by dolomite, is progressively occluded by overdolomitisation, especially in the upper part of the column where the supply of Mg^{2+} is not limited. Overdolomitisation is more effective after calcite has been replaced by dolomite.

Whilst inter-well scale models generate a dolomite distribution in agreement with field observations, regional-scale models reproduce patterns of dolomitisation observed across the Madison ramp only when brine influx is imposed (Simulation 3). A forced influx is however an unrealistic condition given that brine reflux is driven by pressure and density

contrasts and is thus controlled by the distribution of brines of different concentration and by hydraulic parameters (permeability and permeability anisotropy). Injection of brines is a top boundary condition specified by simulations of reflux from a much narrower brine pool by Jones and Xiao (2005). In the Madison case, the specified injection rate allows pervasive dolomitisation beneath the brine pool developed at the top of Sequence I, and minor gypsum precipitation beneath the dolomite body. Models with fluid flow driven by contrasts in fluid density are physically more accurate, but fail to generate a gradient in effective head sufficient to drive significant lateral flux of reactive fluids (Simulation 4). The brines extend less than 1 km down the ramp beyond the edge of the brine pool. Even after diagenetic overprinting during deposition of all three 3rd-order sequences over 3 Myr, and with the brine pool extending across the entire ramp on the top of Sequence III, the head gradient is extremely low and the resulting minimal flow rate significantly limits dolomitisation and any associated diagenetic modification such as gypsum formation. In fact, when assuming a single broad brine pool, as the brine pool extends the average density gradient decreases.

No dolomites form in the distal part of the ramp in any of the regional scale models of the Madison. Despite relatively higher fluxes at the distal edge of the brine pool at the top of Sequence III in respect with fluxes at the edge of the pools in Sequences I and II, the specified brines are less concentrated in distal areas than in the inner ramp. Core and outcrop observations also show a lack of dolomites in outer ramp deposits, with the exception of some dolomitised crinoidal grainstones (Buoniconti, 2008). These dolomites may have formed from geothermal convection of seawater through these areas, or by episodic reflux during short period when there was an overlying brine pool. With their high

internal surface area (Juerges et al., 2016), crinoids would be preferential sites of diagenetic alteration, but they were not assigned a higher RSA in our models.

The fluid fluxes obtained in our 2D stepwise simulations (Simulation 4) are much lower (at least 2 orders of magnitude) than those predicted by previous RTMs of density-driven reflux dolomitisation (Al-Helal et al., 2012a; Lu and Cantrell, 2016). However, the modeled horizontal scale of these platforms is much smaller than that of the Madison (10-35 km *vs* 700 km). Moreover some of these other models specified a much higher permeability anisotropy (1000 ± one order of magnitude) than the model of this study (Al-Helal et al., 2012a). Low flow rates (< 1 m/yr) comparable to those of our simulations are anticipated in flow models of brine reflux in the epeiric-scale Upper Devonian Grosmont platform (455 km long; Jones at al., 2003). In an epeiric ramp such as the Madison, more local-scale flow systems driven by spatial variations in the salinity across the ramp are probably critical in driving reflux dolomitisation. This is demonstrated by simulations using a series of smaller brine pools separated by areas with lower salinity, rather than a singular very broad pool (Simulations 5 and 6). Locally enhanced flow rates cause pervasive dolomitisation at the margin of each pool, with initial preferential alteration of mud-dominated facies. Gypsum always precipitates as a byproduct of dolomitisation, also developing at the margins of each pond and beneath the dolomite bodies.

Changes in climate, sea level and platform-top morphology would lead to lateral migration of the brine pools, resulting in a frequent redistribution of platform-top salinity. Small dolomite bodies formed at different times associated with these migrating ponds could thus eventually coalesce into a larger connected dolomite body (Fig. 14). Small-scale three-dimensional RTM simulations (5 km^2 x 100 m deep) by Xiao et al. (2013) demonstrate that

individual reflux brine plumes sourced by three different ponds (approximately 500 m in diameter) tend to merge into a single plume but heterogeneities in the distribution of initial permeability give rise to a complex dolomite body with 'fingers'. These 3D simulations also demonstrated that refluxing brines can flow up and down depositional dip and along depositional strike. Upward flow of brines as well as downward flow occurs also in our regional scale simulations, at the margins of the brine pools. The classic conceptual model for reflux (*sensu* Saller and Henderson, 1998) envisages a single dolomitisation event resulting in the formation of a simple dolomite body extending basinward the characteristics of which evolve systematically down-flow. A variant of this model, based on the idea of shifting of the brine pond location, has previously been suggested by Lu and Cantrell (2016). These authors explained the occurrence of a non-stratigraphic (non-stratabound) dolomite body in the Jurassic Arab-D reservoir at Ghawar as a result of a series of relatively short-lived reflux episodes generated from a migrating evaporative pool during the falling stage systems tract of the depositional sequence.

Simulations with random variations in brine salinity superimposed on a regional salinity gradient representing increasing restriction towards the ramp interior (Simulation 6), are probably a more realistic representation of reflux systems especially on laterally extensive platforms. Topographic irregularities documented by Buoniconti (2008) and Katz (2008) exert a critical control on platform-top brine distribution. Lake MacLeod in Western Australia provides a modern analogue of a large (*ca.* 130 km long and 40 km wide) and complex coastal salina with spatial variations in salinity (Logan, 1987). Similar variations in micro-topography and resulting variations in residence time of water on the top of ancient carbonate platforms are challenging to reconstruct.

In our simulations with complex salinity distribution, the dolomitisation pattern starts to resemble observations in the Madison, most notably in Sequences I and II where the inner ramp is pervasively dolomitised (after 2 Myr), whilst dolomitisation affects preferentially mud-dominated facies in the mid-ramp. In Sequence III the abundance of dolomite is significantly greater than in simulations without the random variation in brine salinity (Simulation 4; Fig. 15), but dolomitisation is still only partial after an additional 1 Myr of reflux. For such a scenario, even simulations using enhanced dolomite reactive surface area failed to generate the observed dolomitisation pattern (see Fig. C in the online supplemental material), confirming that the system is flux-limited rather than reaction-limited. Our sensitivity analysis shows that specifying permeability anisotropy higher than in the baseline regional scale simulations facilitates lateral flow of brines, which could result in more widespread dolomitisation, resembling even more the actual observations. However, the facies-dependence of dolomitisation is also strongly dependent on RSA, particularly in a flux-limited system. Whilst reconstructing permeability is challenging, the RSA of carbonate sediments and their response to diagenesis is very poorly understood. Even optimizing both these controls (Figs 13 and 15), reflux dolomitisation over epeiric platforms requires overprinting from a series of smaller scale circulation systems set up by spatial variations in brine density.

In this study we simulated only three sequential reflux episodes with brines sourced from lagoons at the top of each 3rd-order sequence boundary. In reality it is probable that brines also developed over shorter periods during high order sea level variations, giving rise to additional overprinting reflux events. Petrographic evidence such as dolomite overgrowths and subtle luminescence zoning described in the Madison dolomudstones and

dolowackestones in mid-to-upper ramp locations (Budd et al., 2006; Katz, 2008) suggests episodic growth thus supporting the hypothesis of iterative reflux rather than a single dolomitisation event. Based on geochemical (O and C stable isotopes and $^{87}Sr/^{86}Sr$) and fluid inclusion data these finely to medium crystalline dolomites were interpreted to have formed from slightly altered Mississippian seawater (Katz, 2008).

The effect of episodic synsedimentary reflux dolomitisation was investigated by Garcia-Fresca (2009) using one-dimensional RTMs representing the deposition of three high frequency cycles of the Albian Upper Glen Rose Formation (central Texas). These simulations demonstrated how dolomitising fluids sourced from younger cycles can flow across stratigraphic boundaries causing the extension and coalescence of multiple dolomite fronts into a vertically continuous dolomite body. Hydrogeologic models of brine reflux in the Permian San Andres Formation coupled with magnesium mass balance between brine and rock also showed that pervasive dolomitisation of carbonate platforms can result by the merging of several dolomite bodies resulting from numerous short-lived reflux episodes sourced in different locations and times (Garcia-Fresca et al., 2012). The amalgamation of small dolomite bodies formed by episodic reflux events into a lager body has been demonstrated as well by RTMs of the same case-study which employed temporally evolving platform geometry and boundary conditions (Palmer et al., 2014).

The reflux model has been invoked to explain pervasive dolomitisation of entire carbonate platforms and sometimes even of entire sedimentary basins, such as for example the Devonian platforms of the Western Canada Sedimentary Basin (Shields and Brady, 1995). However numerical simulations by Jones and Rostron (2000) and Jones et al. (2003) showed that brines discharge onto the platform top within 30 km from their source. In the absence

of a shallow low permeability baffle to discharge, brines could not possibly have extended over the length scale of hundreds of kilometers suggested by the conceptual model of Shields and Brady (1995). Results from this study confirm that the large scale brine reflux across extensive ramps or epeiric platforms is not feasible. As such, large scale brine reflux more likely develops from overprinting by sequential episodes of reflux from multiple small scale brine pools that may shift position over time, rather than from a single very broad pool (Fig. 14).

6. Conclusions

Results from process-based models, including RTMs, are sensitive to and only as meaningful as the way in which the model is set-up. This set of simulations demonstrates both how RTM models of different dimensions and scales can be used to investigate a specific diagenetic problem, and also how results can be strongly determined by the manner in which the model is configured to represent the system. The requirement of modelling to rigorously consider how to quantitatively represent the key elements of the system has highlighted some critical controls which have not previously been explicitly considered. Results from this study suggest that:

- in reflux systems developed on extensive ramps and epeiric platforms, the key controls on diagenesis relate largely to solute supply.
- Reactions, although focused within more reactive units, critically require fluid flow through permeable conduits.
- In addition, the presence of high salinity brines on the platform top is not a guarantee of volumetrically significant reflux, particularly where lateral gradients in

salinity are low. The spatial and temporal distribution of platform-top brines is a key control *via* the resulting gradient in effective head.

- In such flux-limited systems these factors are more important than variations in effective reactive surface area or uncertainties in reaction kinetics.

- Regional-scale dolomitisation of ramp carbonates requires overprinting during successive reflux events.

Acknowledgements

We thank BG Group, Chevron, Petrobras, Saudi Aramco and Wintershall for sponsorship of the University of Bristol ITF (Industry Technology Facilitator) project IRT-MODE. We are grateful to Dr Alina Yapparova and Thomas Palmer for assistance with coding and also thank two anonymous reviewers for their constructive comments and suggestions.

References

Al-Helal, A.B., 2012. Hydrostratigraphic control on early dolomitisation: New insights from process-based modelling. PhD Thesis, University of Bristol, UK.

Al-Helal, A.B., Whitaker, F.F., Xiao, Y., 2012a. Reactive transport modeling of brine reflux: Dolomitization, anhydrite precipitation, and porosity evolution. Journal of Sedimentary Research 82, 196-215.

Al-Helal, A.B., Whitaker, F.F., Spycher, N., Xiao, Y., 2012b. Modeling brine reflux using the Pitzer Ion-Interaction model in Toughreact. Proceedings of the TOUGH Symposium 2012, Lawrence Berkeley National Laboratory, Berkeley, California, pp. 841-847.

Arvidson, R.S., Mackenzie, F.T., 1999. The dolomite problem: Control of precipitation kinetics by temperature and saturation state. American Journal of Science 299, 257-288.

Bennett, R.H., Li, H., Lambert, D.N., Fischer, K.M., Walter, D.J., Hickox, C.E., Hulbert, M.H.,Yamamoto, T., Badiey, M., 1990. In situ porosity and permeability of selected carbonate sediment: Great Bahama bank Part 1: Measurements. Marine Geotechnology 9, 1-28.

Budd, D.A., Pranter, M.J., Reza, Z.A., 2006. Lateral periodic variations in the petrophysical and geochemical properties of dolomite. Geology 34, 373-376.

Budd, D.A., Park, A.J., 2011. Bed-scale reactive transport modeling of dolomitization and the emergence of lateral patterns during dolomitization. In: Engel, A.S., Engel, S., Moore, P., DuChene, H. (Eds.), Carbonate Geochemistry: Reactions and Processes in Aquifers and Reservoirs. Karst Waters Institute, Special Publication 16, pp. 10-13.

Buoniconti, M.R., 2008. The evolution of the carbonate shelf margins and fill of the Antler Foreland Basin by prograding Mississippian carbonates, Northern U.S. Rockies. PhD Thesis, University of Miami, US.

Demicco, R.V., Lowenstein, T.K., Hardie, L.A., Spencer, R.J., 2005. Model of seawater composition for the Phanerozoic. Geology 33, 877-880.

Dickson, A.G., Millero, F.J., 1987. A comparison of the equilibrium-constants for the dissociation of carbonic-acid in seawater media. Deep-Sea Research Part a-Oceanographic Research Papers 34, 1733-1743.

Elrick, M., Read, J.F., 1991. Cyclic ramp-to-basin carbonate deposits, Lower Mississippian, Wyoming and Montana - a combined field and computer modeling study. Journal of Sedimentary Petrology 61, 1194-1224.

Enos, P., Sawatsky, L.H., 1981. Pore networks in Holocene carbonate sediments. Journal of Sedimentary Research 51, 961-985.

Gabellone, T., Whitaker, F., 2016. Secular variations in seawater chemistry controlling dolomitization in shallow reflux systems: insights from reactive transport modelling. Sedimentology 63, 1233-1259 .

Garcia-Fresca, B., Jones, G.D., Tianfu, X., 2009. The apparent stratigraphic concordance of reflux dolomite: New insights from synsedimentary reactive transport models, AAPG Convention, June 7-10, Search and Discovery Article #50208, Denver, Colorado.

Garcia-Fresca, B., Lucia, F.J., Sharp, J.M., Jr., Kerans, C., 2012. Outcrop-constrained hydrogeological simulations of brine reflux and early dolomitization of the Permian San Andres Formation. AAPG Bulletin 96, 1757-1781.

Goldhammer, R.K., 1997. Compaction and decompaction algorithms for sedimentary carbonates. Journal of Sedimentary Research 67, 26-35.

Gutschick, R.C., Sandberg, C.A. , 1983. Mississippian continental margins of the conterminous United States. In: Stanley, D.J., Moore, G.T. (Eds.), The Shelfbreak: Critical Interface on Continental Margins, SEPM Special Publication 33, pp. 79-96.

Haq, B.U., Schutter, S.R., 2008. A chronology of Paleozoic sea-level changes. Science 322(5898), 64-68.

Jones, G.D., Rostron, B.J., 2000. Analysis of fluid flow constraints in regional-scale reflux dolomitization: constant versus variable-flux hydrogeological models. Bulletin of Canadian Petroleum Geology 48, 230-245.

Jones, G.D., Smart, P.L., Whitaker, F.F., Rostron, B.J., Machel, H.G., 2003. Numerical modeling of reflux dolomitization in the Grosmont platform complex (Upper Devonian), Western Canada sedimentary basin. AAPG Bulletin 87, 1273-1298.

Jones, G.D., Xiao, Y.T., 2005. Dolomitization, anhydrite cementation, and porosity evolution in a reflux system: Insights from reactive transport models. AAPG Bulletin 89, 577-601.

Juerges, A., Hollis, C. E., Marshall, J. and Crowley , S., 2016. The control of basin evolution on patterns of sedimentation and diagenesis: an example from the Mississippian Great Orme, North Wales. Journal of the Geological Society 173, 438-456.

Katz, D.A., 2008. Early and late diagenetic processes of Mississippian carbonates, Northern U.S. Rockies. PhD Thesis, University of Miami, US.

Katz, D.A., Eberli, G.P., Swart, P.K., Smith, L.B.Jr., 2006. Tectonic-hydrothermal brecciation associated with calcite precipitation and permeability destruction in Mississippian carbonate reservoirs Montana and Wyoming. AAPG Bulletin 90, 1803-1841.

Land, L.S., 1985. The origin of massive dolomite. Journal of Geological Education 33, 112-125.

Logan, B.W., 1987. The MacLeod evaporite basin, Western Australia: Holocene environments, sediments and geological evolution. AAPG Memoir, 44, Tulsa, OK.

Lu, P., Cantrell, D., 2016. Reactive transport modelling of reflux dolomitization in the Arab-D reservoir, Ghawar field, Saudi Arabia. Sedimentology 63, 865–892.

Lucia, F.J., 1995. Rock-fabric petrophysical classification of carbonate pore-space for reservoir characterization. AAPG Bulletin 79, 1275-1300.

Lucia, F.J., 2007. Carbonate Reservoir Characterization. Springer-Verlag Berlin Heidelberg.

Lucia, F.J., Major, R.P., 1994. Porosity evolution through hypersaline reflux dolomitization. In: Purser, B., Tucker., M., Zenger, D. (Eds.), Dolomites - A volume in honour of Dolomieu. IAS Special Publication 21, Oxford, UK, pp. 325-341.

Machel, H.G., 2004. Concepts and models of dolomitization: a critical reappraisal. In: Braithwaite, C.J.R., Rizzi, G., Darke, G. (Eds.), The Geometry and Petrogenesis of Dolomite Hydrocarbon Reservoirs. Geological Society of London, Special Publication 235, Londond, pp. 7-63.

Markello, J.R., Koepnick, R.B., Waite, L.E., Collins, J.F., 2008. The carbonate analogs through time (CATT) hypothesis and the global atlas of carbonate fields – a systematic and predictive look at Phanerozoic carbonate systems. In: Lukasik, J., Simo, J.A. (Eds.), Controls on Carbonate Platform and Reef Development. SEPM Special Publication 89, Tulsa, OK, pp. 15-45.

Mehrbach, C., Culberso, C.H., Hawley, J.E., Pytkowic, R.M., 1973. Measurement of apparent dissociation-constants of carbonic-acid in seawater at atmospheric-pressure. Limnology and Oceanography 18, 897-907.

Middleton, G.V., 1961. Evaporite solution breccias from the Mississippian of Southwest Montana. Journal of Sedimentary Petrology 31, 189-195.

Moore, C.H., 2001. Carbonate reservoirs: Porosity evolution and diagenesis in a sequence stratigraphic framework. Elsevier, Amsterdam.

Morrow, D.W., 1982. Diagenesis 2. Dolomite – part 2. Dolomitization models and ancient dolostones. Geoscience Canada 9, 95-107.

Palmer, T., Whitaker, F.F., Gabellone, T., Frazer, M.A., Garcia-Fresca, B., 2014. Evaluating links between sequence stratigraphy and reflux dolomitisation of the Permian San Andres Formation, AAPG Annual Conference and Exhibition, April 6-9, Search and Discovery Article #90189, Houston, TX.

Parkhurst, D.L., Appelo, C.A.J., 1999. User's guide to PHREEQC (version 2) - A computer program for speciation, batch-reaction, one-dimensional transport, and inverse geochemical calculations. U.S. Geological Survey Water-Resources Investigations Report 99-4259.

Pierrot, D., Lewis, E., Wallace, D., 2006. MS Excel Program developed for CO_2 system calculations, Carbon Dioxide Information analysis Center. Oak Ridge National Laboratory, US Department of Energy, Oak Ridge, Tennessee, US.

Roberts, A.E., 1966. Stratigraphy of Madison Group near Livingston, Montana, and discussion of karst and solution-breccia features. USGS Professional Paper 526-B.

Saller, A.H., Henderson, N., 1998. Distribution of porosity and permeability in platform dolomites: Insight from the Permian of West Texas. AAPG Bulletin 82, 1528-1550.

Shields, M.J., Brady, P.V., 1995. Mass-balance and fluid-flow constraints on regional-scale dolomitization, Late Devonian, Western Canada Sedimentary Basin. Bulletin of Canadian Petroleum Geology 43, 371-392.

Smart, P.L., Waltham D.A., Felce, G.P., Whitaker, F.F. (2005). CARB3D+: A new forward simulation model for sedimentary architecture and near-surface diagenesis in isolated carbonate platforms. AAPG International Conference, September 11-14, Search and Discovery Article #90046, Paris, France.

Smith, L.B.J., Eberli , G.P., Sonnenfeld, M., 2004. Sequence-stratigraphic and paleogeographic distribution of reservoir-quality dolomite, Madison Formation, Wyoming and Montana. In: Grammer, G.M., Harris, P.M., Eberli, G.P. (Eds.), Integration of outcrop and modern analogs in reservoir modeling. AAPG Memoir 80, pp. 67– 92.

Sonnenfeld, M.D., 1996a. An integrated sequence stratigraphic approach to reservoir characterization of the Lower Mississippian Madison Limestone, emphasizing Elk Basin field, Bighorn Basin, Wyoming. PhD Thesis, Colorado School of Mines, Golden, Colorado, US.

Sonnenfeld, M.D., 1996b. Sequence evolution and hierarchy within the Lower Mississippian Madison limestone of Wyoming. In: Longman, M.W., Sonnenfeld, M.D. (Eds.), Paleozoic Systems of the Rocky Mountain Region. Rocky Mountain Section, SEPM Special Publication, Denver, CO, pp. 165-192.

Stanton, R.J., Jeffery, D.L., Ahr, W.M., 2002. Early Mississippian climate based on oxygen isotope compositions of brachiopods, Alamogordo Member of the Lake Valley

Formation, south-central New Mexico. Geological Society of America Bulletin 114, 4-11.

Sun, S.Q., 1995. Dolomite reservoirs - porosity evolution and reservoir characteristics. AAPG Bulletin 79, 186-204.

Wahlman, G.P., 2010. Reflux dolomite crystal size variation in cyclic inner ramp reservoir facies, Bromide Formation (Ordovician), Arkoma Basin, Southeastern Oklahoma. The Sedimentary Record 8, 4-9.

Wardlaw, N.C., 1976. Pore geometry of carbonate rocks as revealed by pore casts and capillary pressure. AAPG Bulletin 60, 245-257.

Warren, J.K., 1999. Evaporites: their evolution and economics. Blackwell Scientific, Oxford, UK.

Warren, J.K., 2000. Dolomite: occurrence, evolution and economically important associations. Earth-Science Reviews 52, 1-81.

Whitaker, F.F., Xiao, Y., 2010. Reactive transport modeling of early burial dolomitization of carbonate platforms by geothermal convection. AAPG Bulletin 94, 889-917.

Woody, R.E., Gregg, J.M., Koederitz, L.F., 1996. Effect of texture on petrophysical properties of dolomite: Evidence from the Cambrian-Ordovician of southeastern Missouri. AAPG Bulletin 80, 119-132.

Xiao, Y., Jones, G.D, Whitaker, F.F. , Al-Helal, A.B, Stafford, S., Gomez-Rivas, E., Guidry, S., 2013. Fundamental approaches to dolomitisation and carbonate diagenesis in different hydrogeological systems and the impact on reservoir quality distribution. International Petroleum Technology Conference, Beijing, China, pp. 1164-1179.

Xu, T.F., Sonnenthal, E., Spycher, N., Pruess, K., 2004. TOUGHREACT user's guide: A simulation program for non-isothermal multiphase reactive geochemical transport in variable saturated geologic media: Lawrence Berkeley National Laboratory Report LBNL-55460, Berkeley, CA.

Zahm, C., Kerans, C., El-Azzi, J., and Eldam, N., 2015. Evaporite paleokarst on a tectonically enhanced unconformity, Mississippian Madison Formation, Wyoming, USA. AAPG Annual Convention and Exhibition, May 31 - June3, Search and Discovery Article #90216, Denver, Colorado.

Zeebe, R.E., 2012. History of seawater carbonate chemistry, atmospheric CO_2, and ocean acidification. Annual Review of Earth and Planetary Sciences 40, 141-165.

Table and figure captions

Table 1. Rock properties.

Table 2. Summary of key features of simulations.

Fig. 1. Paleogeography of the western United States in the Early Mississippian. The Madison Formation was part of an extensive carbonate ramp that extended from Illinois to New Mexico and northward to Canada. Lines AA'-A'-A'' are the lines of section for the high-resolution sequence stratigraphic cross section of Fig. 2. HC=Hartville Canyon; Liv=Livingston; Mon=Monarch; SM=Sheep Mountain. Modified from Sonnenfeld (1996b) and Gutschick and Sandberg (1983).

Fig. 2. A) Sequence stratigraphic cross section along AA'-A'-A'' in Fig. 1 (modified after Sonnenfeld, 1996b), summarising 3rd-order sequence evolution. HC=Hartville Canyon;

SM=Sheep Mountain; Liv=Livingston; Mon=Monarch. The sedimentary architecture and the rock properties between Livingston and Monarch are simplified, and are based on the facies distribution of Buoniconti (2008). B) Dolomite and limestone distribution in the Madison Formation (modified after Smith et al. 2004 and Katz, 2008).Fig. 3. Rock properties. A) Distribution of rock types within regional scale simulation grid. Dashed lines represent the sequence boundaries. B) Depth dependence of initial porosity for each rock type, based on fraction of fines (ff). C) Porosity-permeability relationships and D) estimated reactive surface area (RSA), for each rock type.

Fig. 4. 1D and 2D inter-well scale model set-up. A) Decompacted stratigraphy of Sequence I at the Sheep Mountain outcrop (modified after Smith et al. 2004). B) Depth-dependence of initial permeability and C) of effective reactive surface area.

Fig. 5. Grid, boundary conditions and salinity specification for 2D regional scale simulations. A) Simulation 3. B) Simulations 4, 5 and 6. In these three sets of simulations we model stepwise accumulation and flow through Sequences I, II and III with changing distribution of brine salinity across of the top of the ramp through the three Sequences (see Fig. 6 for location of brine pools). C) In Simulations 3 and 4 brine salinity increases linearly towards the ramp interior, but in Sequence III remains a constant 142 ‰ in the inner ramp. D) In Simulation 6 brine salinity varies randomly ± 70 ‰ around the linear trends of Fig. 5C.

Fig. 6. Initial rock properties for Simulations 4, 5 and 6 (2D regional scale with density driven flow). Black triangles and bars show salinity (in ‰) within the brine pools at the top of Sequences I (A), II (B) and III (C) for Simulations 4 and 5 respectively. In Simulation 4 brine salinity is progressively more concentrated towards the inner ramp, whilst in Simulation 5 each pond has a different brine salinity and is separated by an area of normal marine

seawater (35 ‰). Dashed lines correspond to sequence boundaries. RSA= Reactive surface area. See Fig. 5D for brine salinity distribution in Simulation 6.

Fig 7. Results of 1D inter-well scale models (Simulation 1). A) Decompacted stratigraphy of Sequence I at the Sheep Mountain outcrop. B-E) Evolution of dolomite abundance (% of total solid) over 1 Myr of vertical brine reflux for four different brine injection rates. Dolomitisation initially affects only the more reactive beds and those at shallower depth, and subsequently becomes pervasive, more rapidly at high brine flux. Note that the bottom cell has fixed properties and thus it is not displayed. F-M) Changes in mineralogy and porosity (volume fraction) over 1 Myr predicted at depths of 0.3 m (F-I) and 35 m (J-M; black arrows in B) for four different injection rates.

Fig. 8. Results of 2D inter-well scale models (Simulation 2). A) Decompacted stratigraphy of Sequence I at the Sheep Mountain outcrop. B) Flow velocity after 200 kyr of lateral brine reflux assuming an inflow across the right boundary equivalent to reflux at 0.01 m/yr across the 180 km wide brine pool at the top of Sequence I (Fig. 8A). C-D) Extracted 1D data at x=1500 m showing temporal evolution of dolomite abundance (% of total solid) over 1Myr of brine reflux based on a reflux at 0.01 (C) and 0.001 m/yr (D). Flow is focussed in more permeable coarse grained beds, providing reactants for strongly preferential alteration of adjacent more reactive fine grained beds.

Fig. 9. Initial rock properties (A and B) and results of 2D regional scale models of Sequence I, focussing on the inner ramp (frame in Fig. 11A) after 1 Myr of brine injection at a constant rate of 0.001 m/yr (C,E and G; Simulation 3) and density driven brine inflow (D, F and H; Simulation 4) from a 180 km wide brine pool (black triangle above platform top). Brine salinity increases linearly from the margin of the pool towards the ramp interior. Plots of

fluid flux use a log scale; note change in scale in D compared to C. Dolomite abundance is in % of the total solid, using a log scale. Rock type key is the same as for Fig. 3.

Fig. 10. Initial porosity (A) and porosity changes due to dolomitisation (B) in the inner ramp of Sequence I after 1 Myr of simulated brine reflux (Simulation 3). The black line in B shows the 90% dolomite contour. Porosity increases are due to dolomitisation (replacement of calcite), and overdololomitisation (dolomite cementation) is not occurring.

Fig. 11. Results of 2D regional scale models of density driven reflux (Simulation 4) of brines sourced from pools (black triangles) on the top of Sequences I (A-C), II (D-F) and III (G-I). Dashed lines correspond to sequence boundaries. The simulated duration of reflux in each sequence is 1Myr. The frame in A is enlarged in Fig. 9D. Dolomite abundance is in % of the total solid, using a log scale.

Fig. 12. Initial rock properties (A and E) and results of 2D regional scale models of density driven reflux sourced from 5 brine pools (black bars at the top; B-E; Simulation 5), and with a random brine salinity distribution shown in Fig. 5 (F-J; Simulation 6). Dashed lines correspond to sequence boundaries. The total simulated duration of reflux for the three sequences is 3 Myr. Dolomite abundance is in % of the total solid, using a log scale.

Fig. 13. 2D regional scale models showing sensitivity of reflux dolomitisation to reactive surface area (RSA) and permeability anisotropy (reflecting changes in K_h) for Simulation 6 after 1 Myr reflux affecting Sequence I. Simulations use permeability anisotropy and RSA of 1 and 2 orders of magnitude respectively higher than values shown in the baseline (Fig. 12 A and E). For each simulation the flux of brines into the platform after 1 Myr simulation time is given in kg/yr.

Fig. 14. Conceptual model of dolomitisation by brine reflux in a prograding epeiric-scale carbonate ramp. Topographic irregularities on the ramp top control brine generation by evaporation and thus reflux during ramp evolution. Dolomitisation associated with each brine pool preferentially affects underlying and adjacent fine grained sediments. Over time, dolomite abundance increases, dolomite develops in less reactive coarse grained sediments and dolomite pods amalgamate.

Fig. 15. A) Histogram showing the abundance of dolomite within the cross-sectional area for Simulation 3. B) Comparison of area of dolomite (>90% dolomite), calcitic dolomite (50-90% dolomite), dolomitic limestone (10-50% dolomite) and limestone (<10% dolomite) generated during all simulations. Note cross-section area increases from 21 km^2 for Sequence I to 30 and 44 km^2 for Sequences II and III respectively. The cross section extends into the basin where large areas are never affected by refluxing brines and remain limestone (Fig. 2B). Gypsum is excluded from quantitative calculations.

Fig. A - online supplementary material: Gypsum abundance (% of total solid) in different 2D regional scale RTMs. A) Brine injection in the innermost ramp of Sequence I (Simulation 3). The time simulated is 1Myr. B) Density driven flow in Sequences I-III from a single brine pool at the top of each sequence (Simulation 4), from 5 brine pools in each sequence (C; Simulation 5) , and with random brine salinity distribution across the top of each sequence (D; Simulation 6). Dashed lines correspond to sequences boundaries. The total simulated duration of reflux for the three sequences is 3 Myr.

Fig. B – online supplementary material. Temperature evolution and brine flow through Sequences I, II and III during stepwise accumulation.

Fig C. – online supplementary material. Results of 2D regional scale models of density driven reflux with a random brine salinity distribution (Simulation 6). Simulations in A and B use a reactive surface area (RSA) 1 and 2 orders of magnitude respectively higher than values which are used in the baseline (Fig. 12A, E-H). Dashed lines correspond to sequence boundaries. The total simulated duration of reflux for the three sequences is 3 Myr. Dolomite abundance is in % of the total solid, using a log scale.

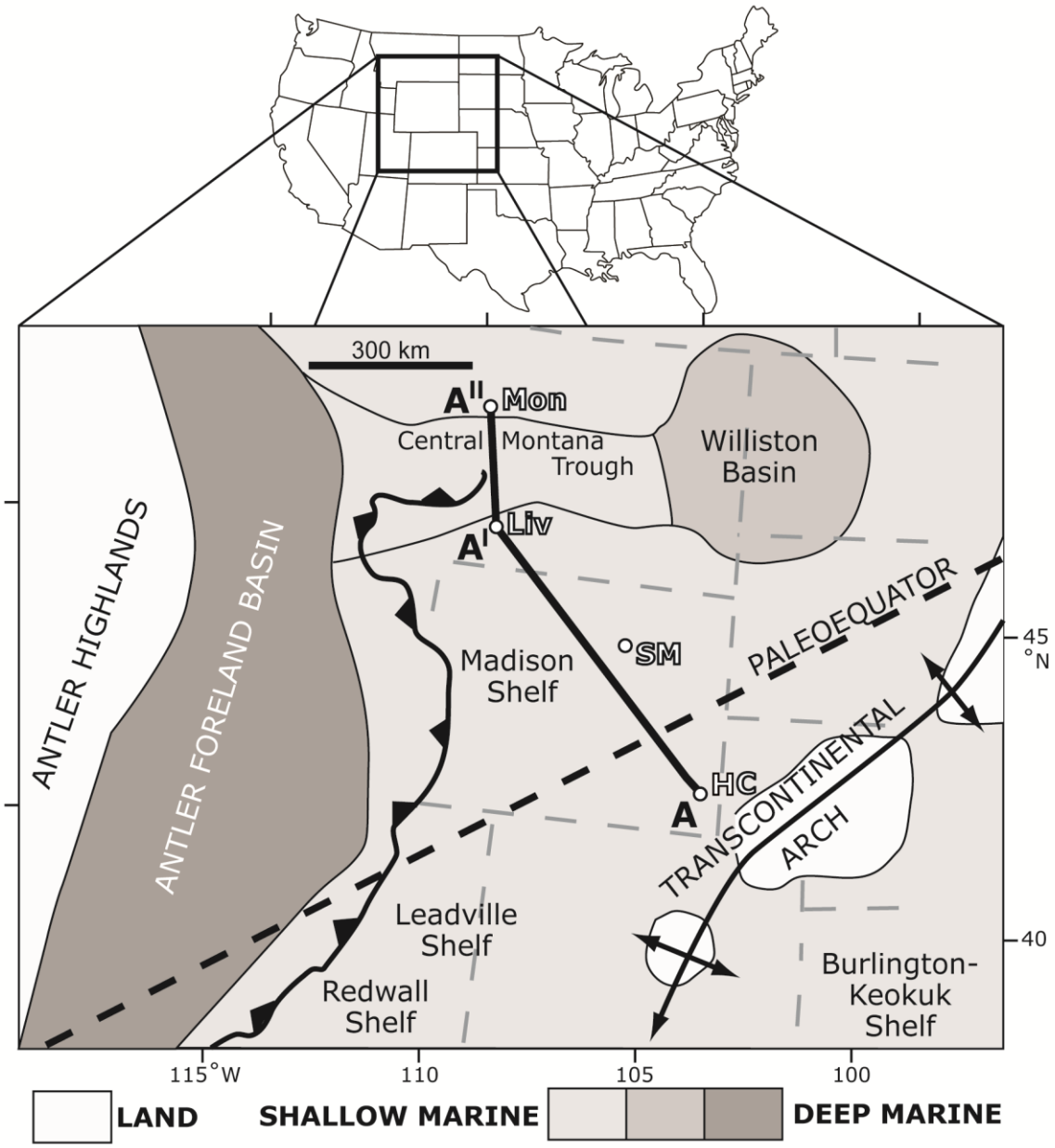
300 km
A''
Mon
Central Montana Trough
Williston Basin
A'
Liv
ANTLER HIGHLANDS
ANTLER FORELAND BASIN
Madison Shelf
SM
PALEOEQUATOR
45 °N
HC
A
TRANSCONTINENTAL ARCH
Leadville Shelf
Redwall Shelf
Burlington-Keokuk Shelf
40
115°W
110
105
100
LAND
SHALLOW MARINE
DEEP MARINE

Fig. 1

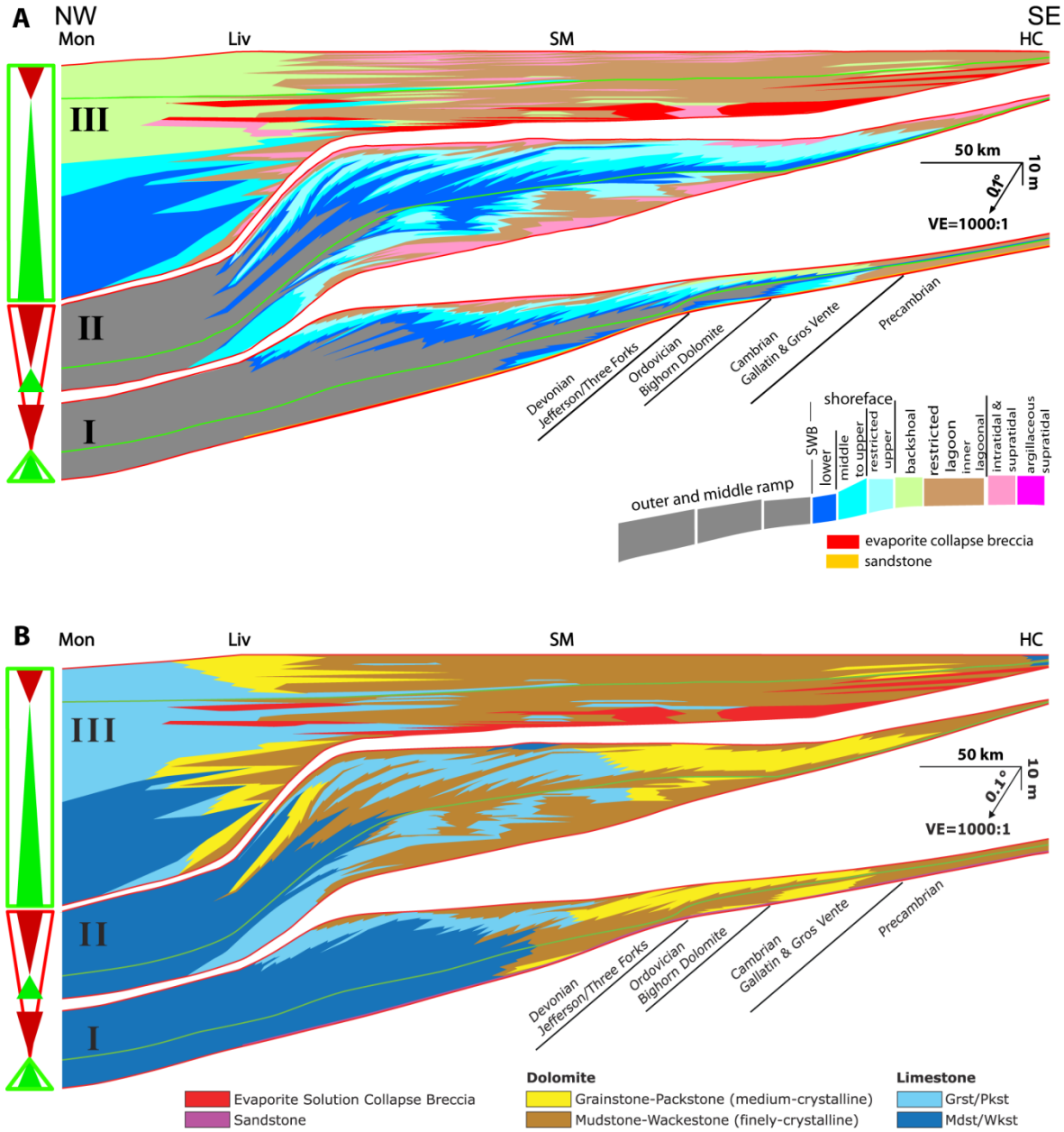
A
NW
SE
Mon
Liv
SM
HC
III
II
I
50 km
10 m
0.1°
VE=1000:1
Devonian
Jefferson/Three Forks
Ordovician
Bighorn Dolomite
Cambrian
Gallatin & Gros Vente
Precambrian
shoreface
SWB
lower
middle
to upper
restricted
upper
backshoal
restricted
lagoon
inner
lagoonal
intratidal &
supratidal
argillaceous
supratidal
outer and middle ramp
evaporite collapse breccia
sandstone
B
Mon
Liv
SM
HC
III
II
I
50 km
10 m
0.1°
VE=1000:1
Devonian
Jefferson/Three Forks
Ordovician
Bighorn Dolomite
Cambrian
Gallatin & Gros Vente
Precambrian
Evaporite Solution Collapse Breccia
Sandstone
Dolomite
Grainstone-Packstone (medium-crystalline)
Mudstone-Wackestone (finely-crystalline)
Limestone
Grst/Pkst
Mdst/Wkst

Fig. 2

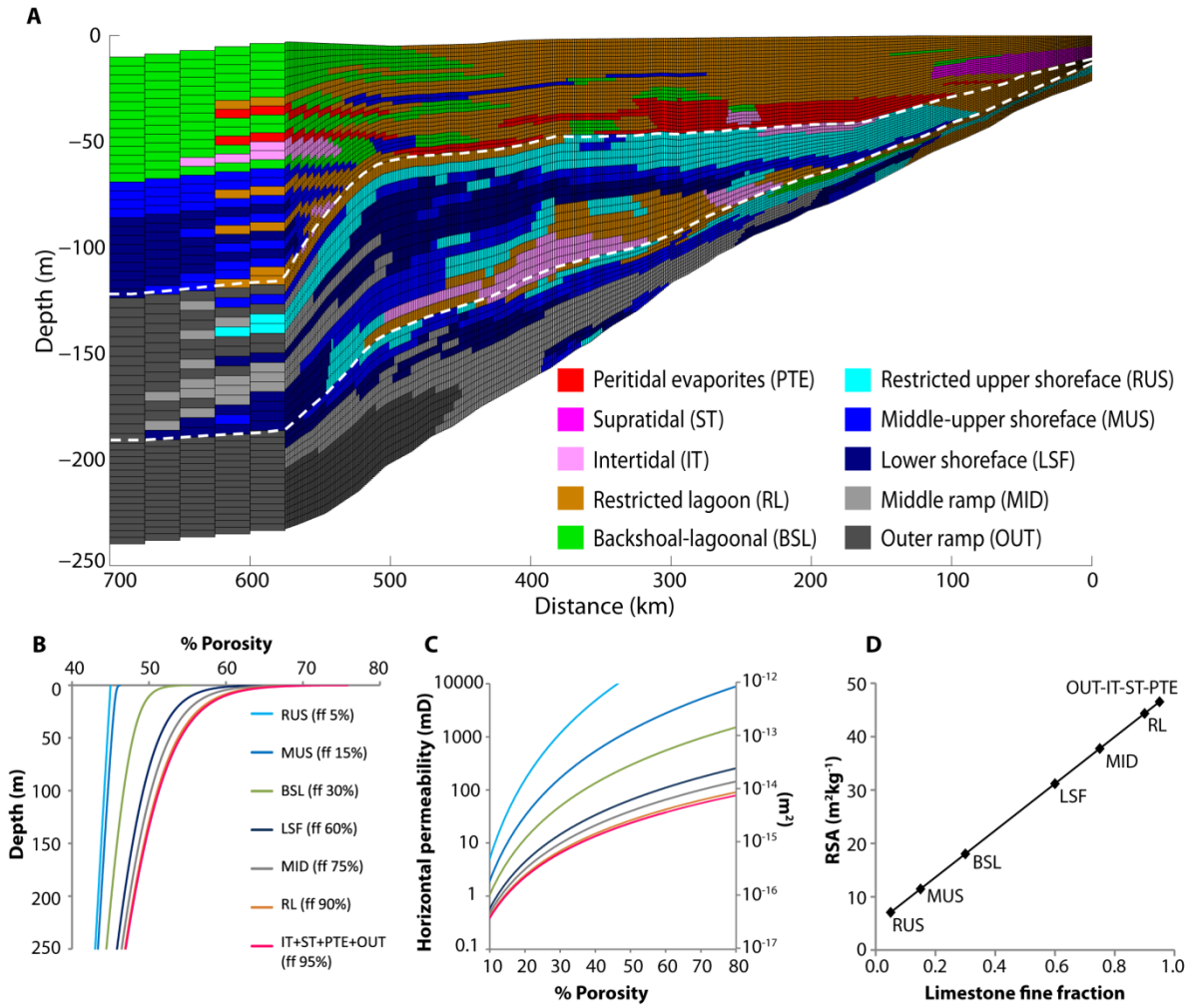
A
Depth (m)
Distance (km)
Peritidal evaporites (PTE)
Supratidal (ST)
Intertidal (IT)
Restricted lagoon (RL)
Backshoal-lagoonal (BSL)
Restricted upper shoreface (RUS)
Middle-upper shoreface (MUS)
Lower shoreface (LSF)
Middle ramp (MID)
Outer ramp (OUT)
B
% Porosity
Depth (m)
RUS (ff 5%)
MUS (ff 15%)
BSL (ff 30%)
LSF (ff 60%)
MID (ff 75%)
RL (ff 90%)
IT+ST+PTE+OUT (ff 95%)
C
Horizontal permeability (mD)
% Porosity
D
RSA (m²kg⁻¹)
Limestone fine fraction
OUT-IT-ST-PTE
RL
MID
LSF
BSL
MUS
RUS

Fig. 3

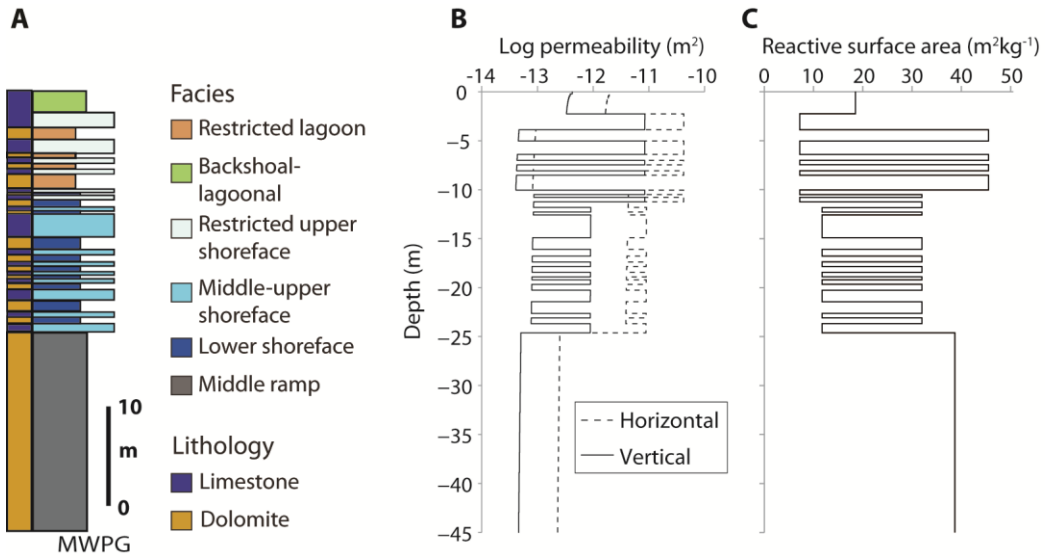
A
Facies
Restricted lagoon
Backshoal-lagoonal
Restricted upper shoreface
Middle-upper shoreface
Lower shoreface
Middle ramp
Lithology
Limestone
Dolomite
10
m
0
MWPG
B
Log permeability (m²)
-14 -13 -12 -11 -10
Depth (m)
0 −5 −10 −15 −20 −25 −30 −35 −40 −45
Horizontal
Vertical
C
Reactive surface area (m²kg⁻¹)
0 10 20 30 40 50

Fig. 4

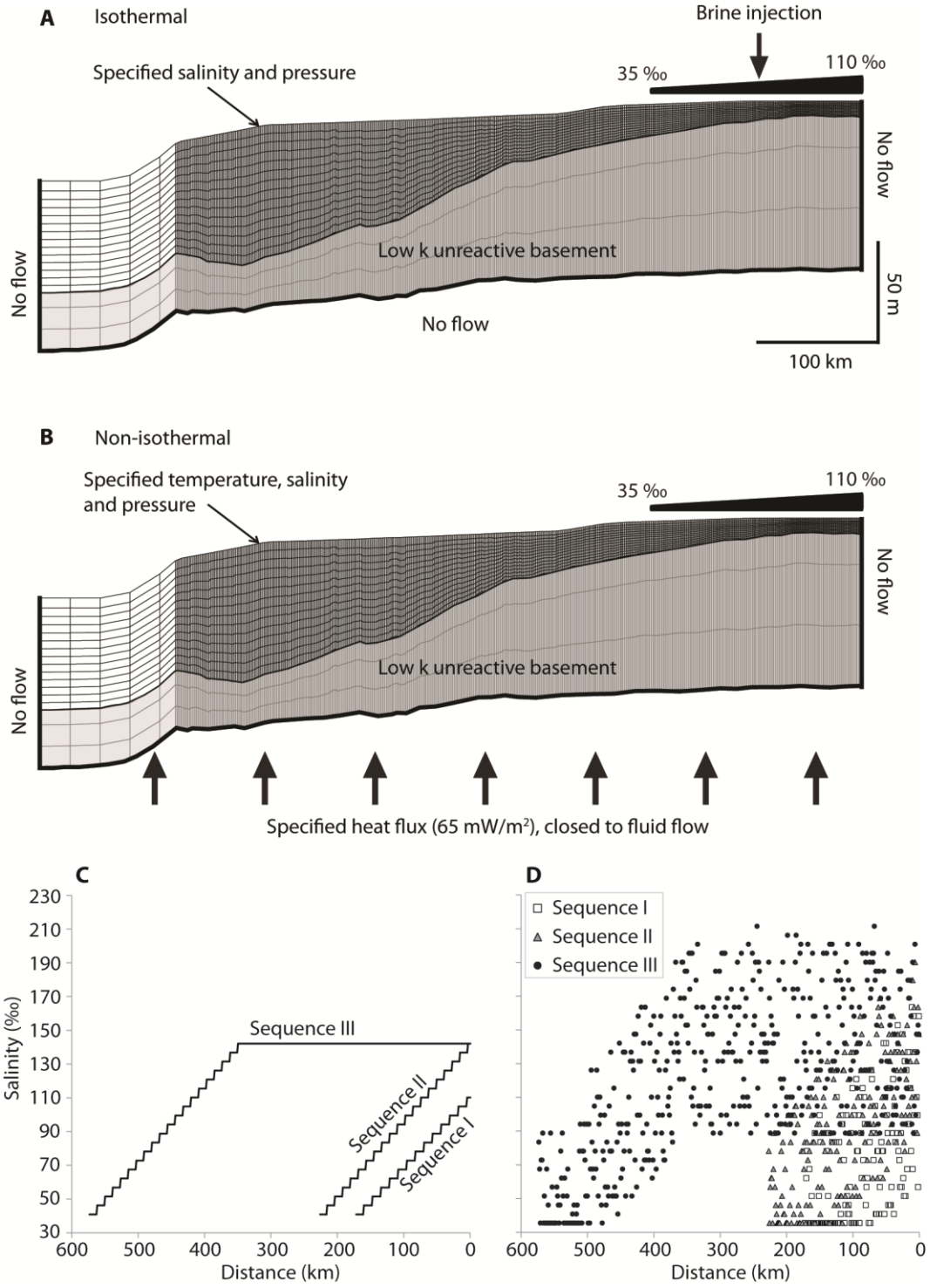
A
Isothermal
Brine injection
Specified salinity and pressure
35 ‰
110 ‰
No flow
Low k unreactive basement
No flow
No flow
50 m
100 km
B
Non-isothermal
Specified temperature, salinity and pressure
35 ‰
110 ‰
No flow
Low k unreactive basement
No flow
Specified heat flux (65 mW/m²), closed to fluid flow
C
Salinity (‰)
Sequence III
Sequence II
Sequence I
Distance (km)
D
Sequence I
Sequence II
Sequence III
Distance (km)

Fig. 5

Fig. 6

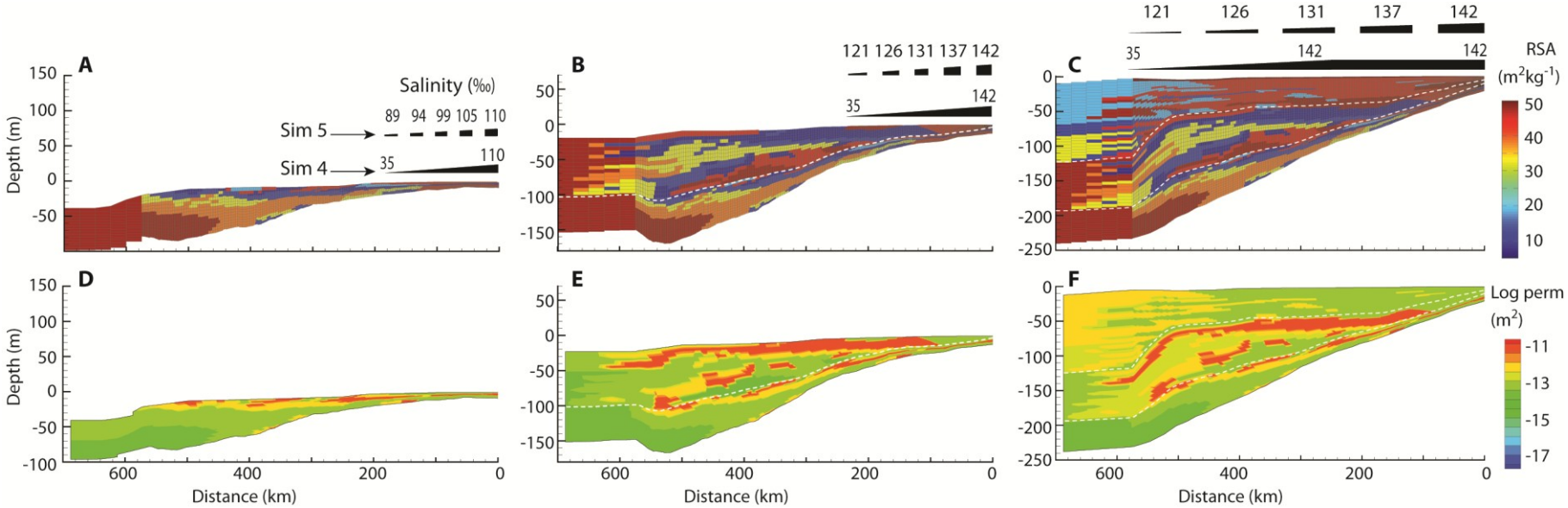
A
B
C
D
E
F
Salinity (‰)
Sim 5
Sim 4
89 94 99 105 110
35
110
121 126 131 137 142
35
142
121 126 131 137 142
35
142
142
RSA
(m²kg⁻¹)
50
40
30
20
10
Log perm
(m²)
-11
-13
-15
-17
Depth (m)
Distance (km)
600
400
200
0

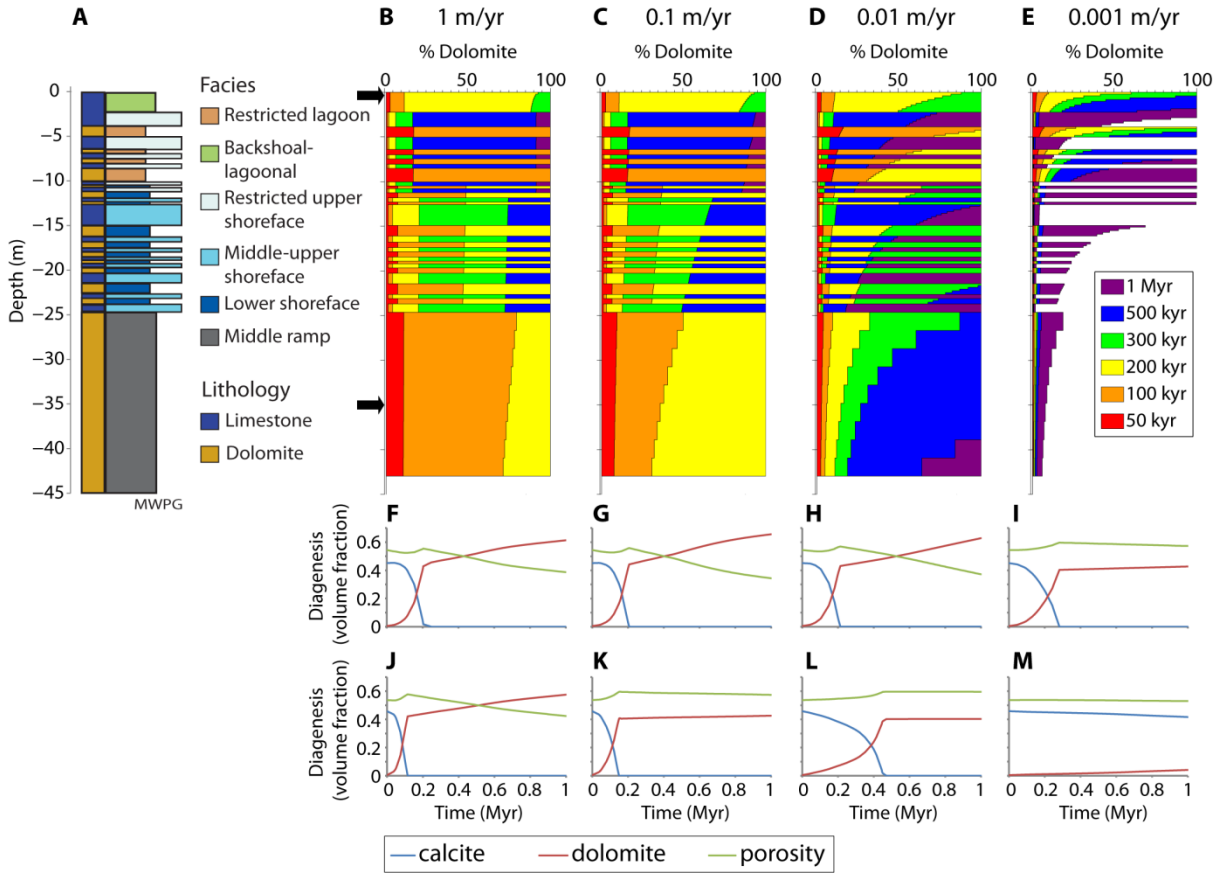
A
B 1 m/yr
C 0.1 m/yr
D 0.01 m/yr
E 0.001 m/yr
% Dolomite
0
50
100
Depth (m)
0
−5
−10
−15
−20
−25
−30
−35
−40
−45
MWPG
Facies
Restricted lagoon
Backshoal-lagoonal
Restricted upper shoreface
Middle-upper shoreface
Lower shoreface
Middle ramp
Lithology
Limestone
Dolomite
1 Myr
500 kyr
300 kyr
200 kyr
100 kyr
50 kyr
F
G
H
I
J
K
L
M
Diagenesis (volume fraction)
0
0.2
0.4
0.6
0.8
1
Time (Myr)
calcite
dolomite
porosity

Fig. 7

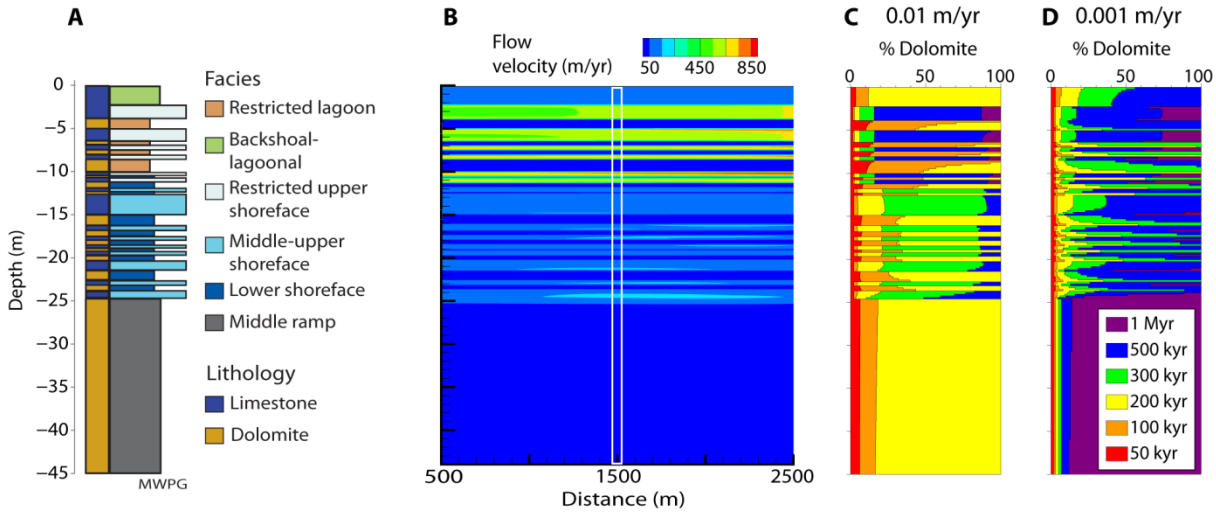
A
B
C 0.01 m/yr
D 0.001 m/yr
Depth (m)
0
−5
−10
−15
−20
−25
−30
−35
−40
−45
MWPG
Facies
Restricted lagoon
Backshoal-lagoonal
Restricted upper shoreface
Middle-upper shoreface
Lower shoreface
Middle ramp
Lithology
Limestone
Dolomite
Flow velocity (m/yr)
50 450 850
500
1500
2500
Distance (m)
% Dolomite
0 50 100
% Dolomite
0 50 100
1 Myr
500 kyr
300 kyr
200 kyr
100 kyr
50 kyr

Fig. 8

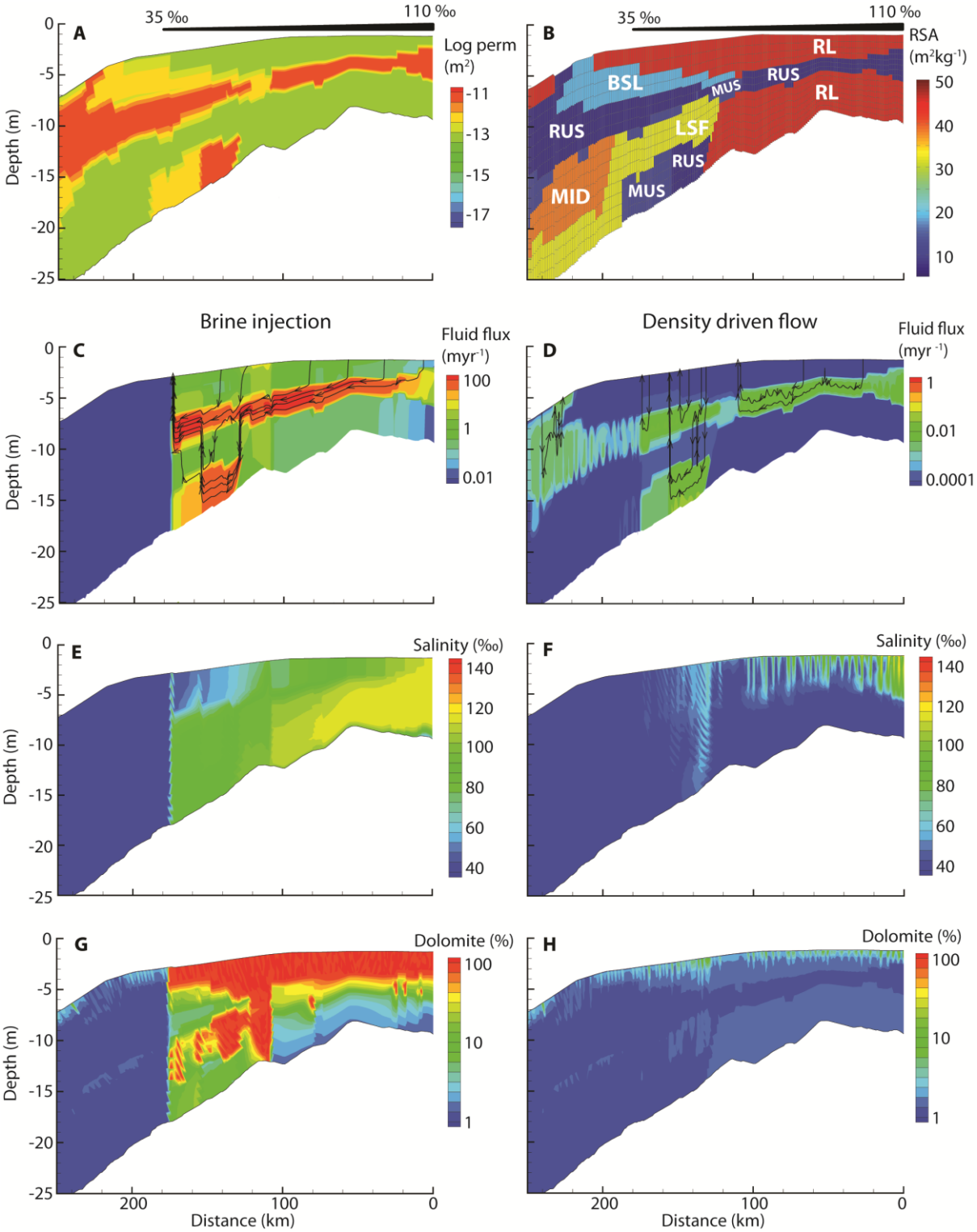
A
35 ‰
110 ‰
Log perm (m²)
-11
-13
-15
-17
Depth (m)
B
RSA (m²kg⁻¹)
50
40
30
20
10
RL
BSL
MUS
RUS
RL
RUS
LSF
RUS
MID
MUS
Brine injection
C
Fluid flux (myr⁻¹)
100
1
0.01
Density driven flow
D
Fluid flux (myr⁻¹)
1
0.01
0.0001
E
Salinity (‰)
140
120
100
80
60
40
F
Salinity (‰)
G
Dolomite (%)
100
10
1
H
Dolomite (%)
200
100
0
Distance (km)

Fig. 9

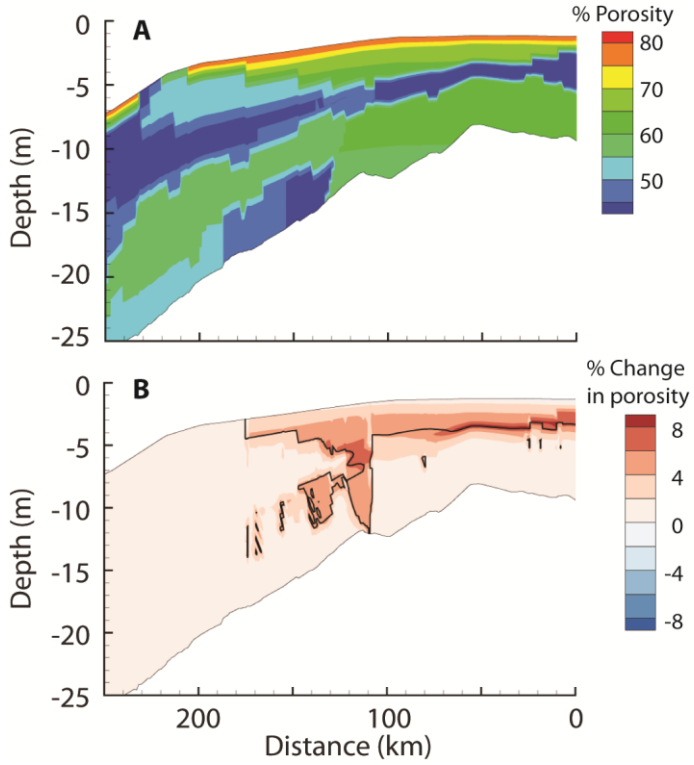
A
% Porosity
80
70
60
50
0
-5
-10
-15
-20
-25
Depth (m)
B
% Change
in porosity
8
4
0
-4
-8
200
100
0
Distance (km)

Fig. 10

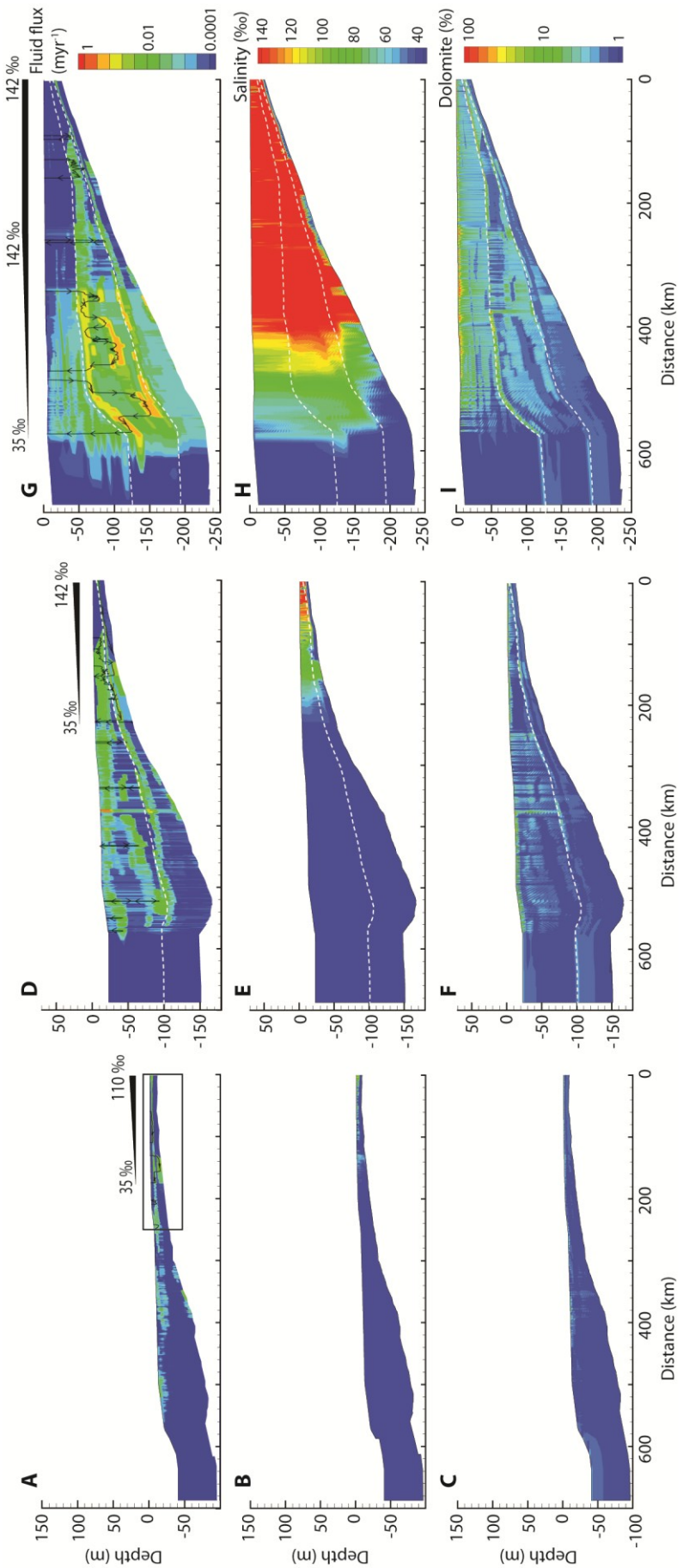
A
B
C
D
E
F
G
H
I
Depth (m)
Distance (km)
110 ‰
35 ‰
142 ‰
Fluid flux (myr⁻¹)
Salinity (‰)
Dolomite (%)

Fig. 11

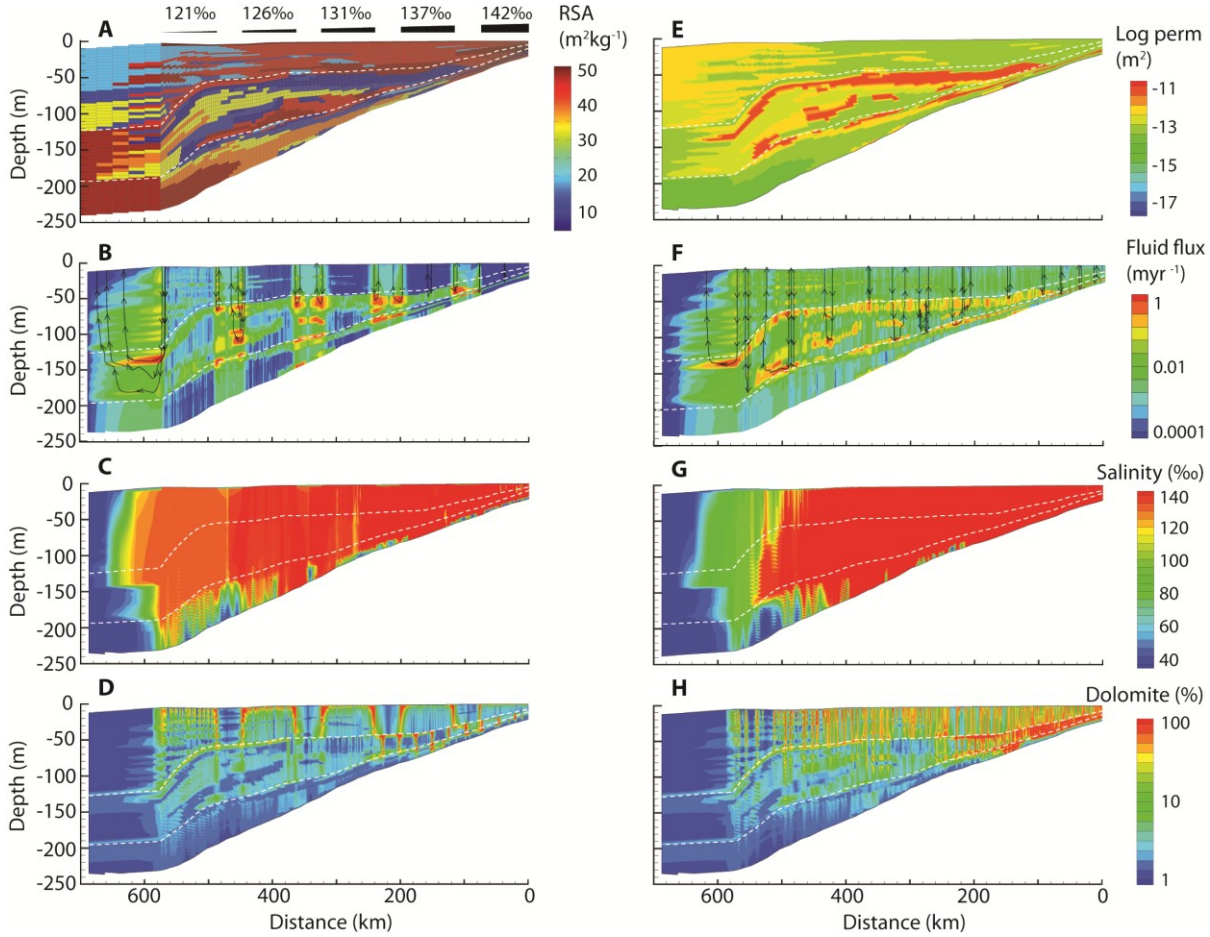
A
121‰
126‰
131‰
137‰
142‰
RSA
(m²kg⁻¹)
50
40
30
20
10
E
Log perm
(m²)
-11
-13
-15
-17
B
F
Fluid flux
(myr⁻¹)
1
0.01
0.0001
C
G
Salinity (‰)
140
120
100
80
60
40
D
H
Dolomite (%)
100
10
1
Depth (m)
0
-50
-100
-150
-200
-250
600
400
200
0
Distance (km)

Fig. 12

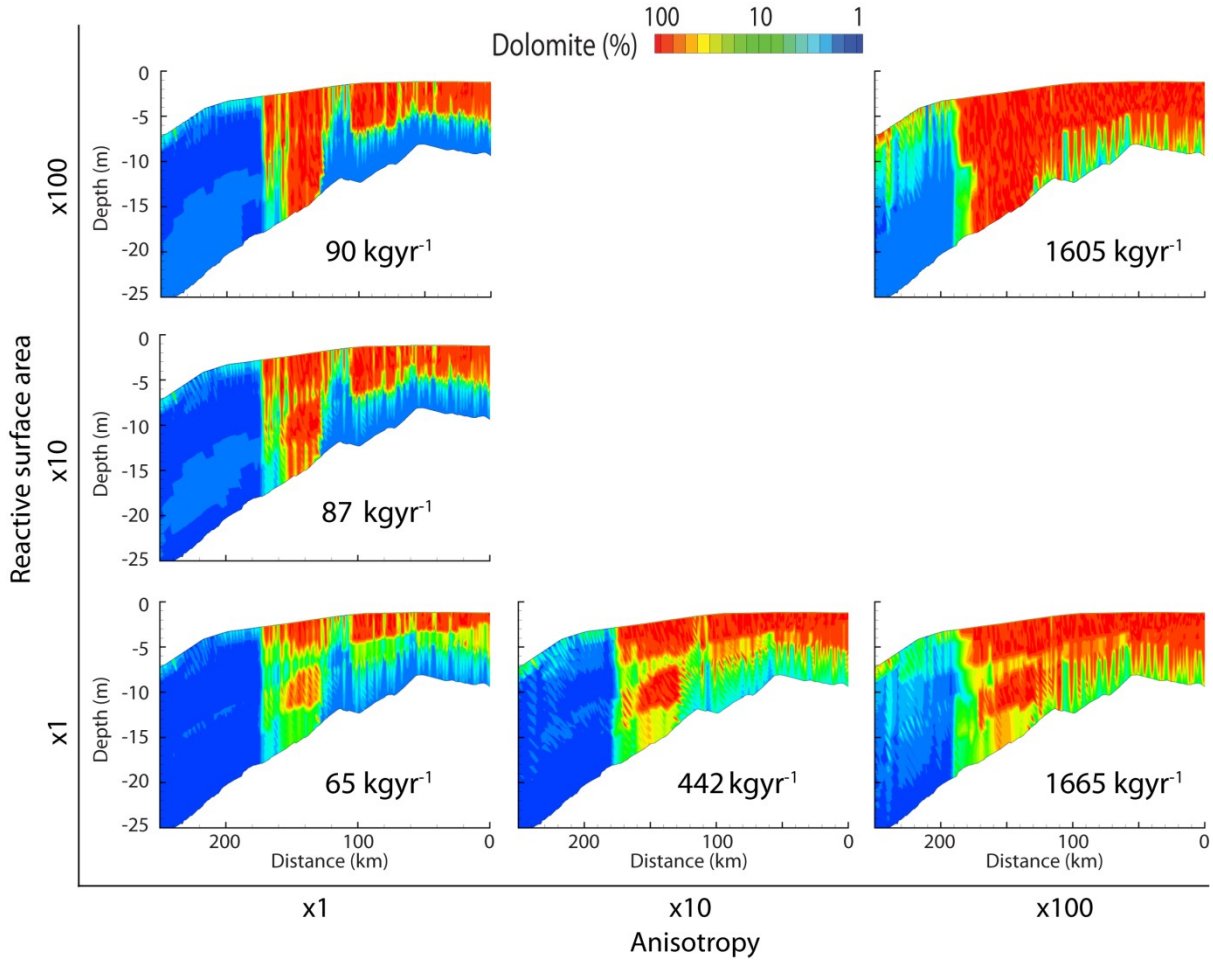
Dolomite (%)
100
10
1
Reactive surface area
x100
x10
x1
Depth (m)
0
-5
-10
-15
-20
-25
90 kgyr-1
1605 kgyr-1
87 kgyr-1
65 kgyr-1
442 kgyr-1
1665 kgyr-1
200
100
0
Distance (km)
x1
x10
x100
Anisotropy

Fig. 13

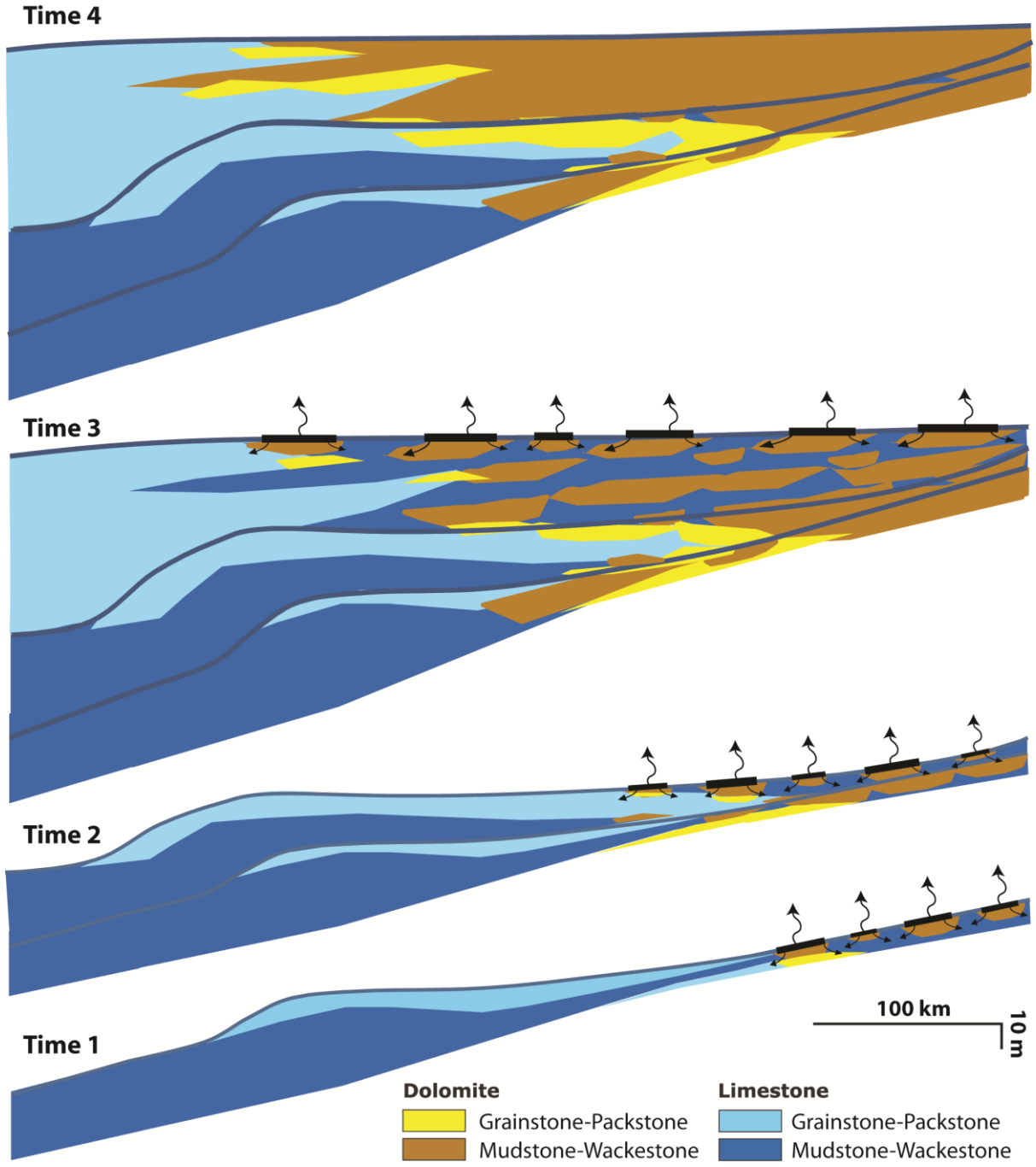
Time 4
Time 3
Time 2
Time 1
100 km
10 m
Dolomite
Grainstone-Packstone
Mudstone-Wackestone
Limestone
Grainstone-Packstone
Mudstone-Wackestone

Fig. 14

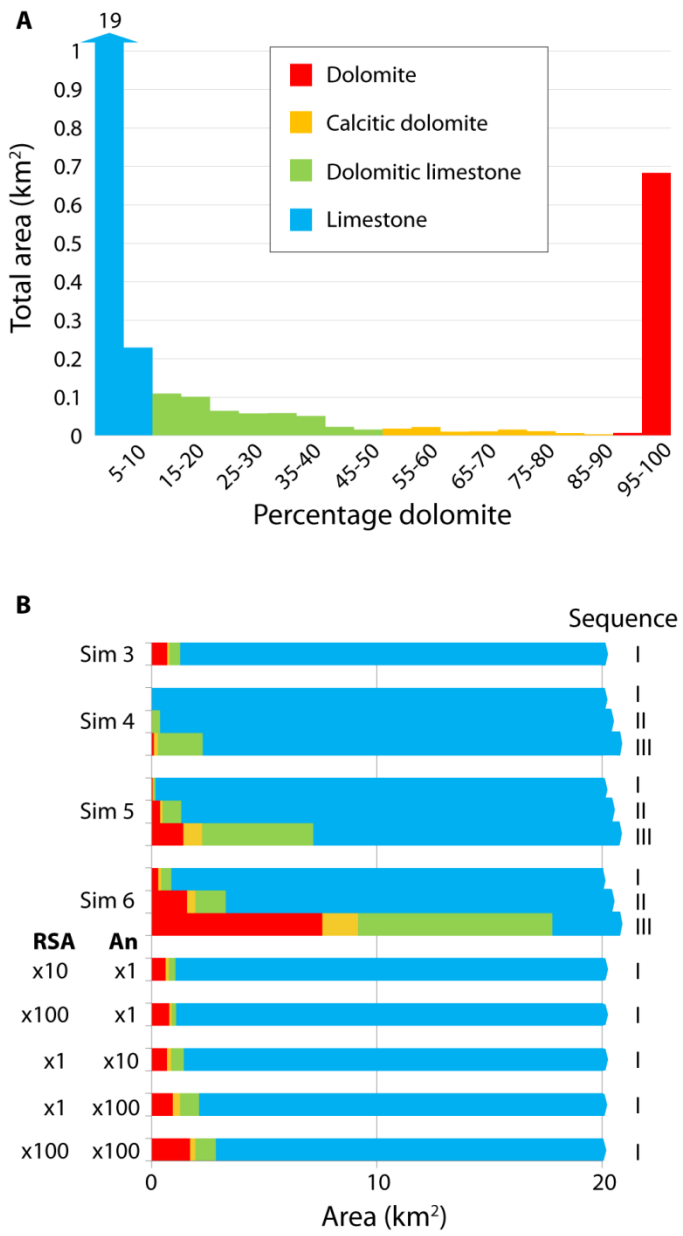
A
19
Total area (km²)
1
0.9
0.8
0.7
0.6
0.5
0.4
0.3
0.2
0.1
0
Dolomite
Calcitic dolomite
Dolomitic limestone
Limestone
5-10
15-20
25-30
35-40
45-50
55-60
65-70
75-80
85-90
95-100
Percentage dolomite
B
Sequence
Sim 3
Sim 4
Sim 5
Sim 6
I
II
III
RSA
An
x10 x1
x100 x1
x1 x10
x1 x100
x100 x100
0
10
20
Area (km²)

Fig. 15

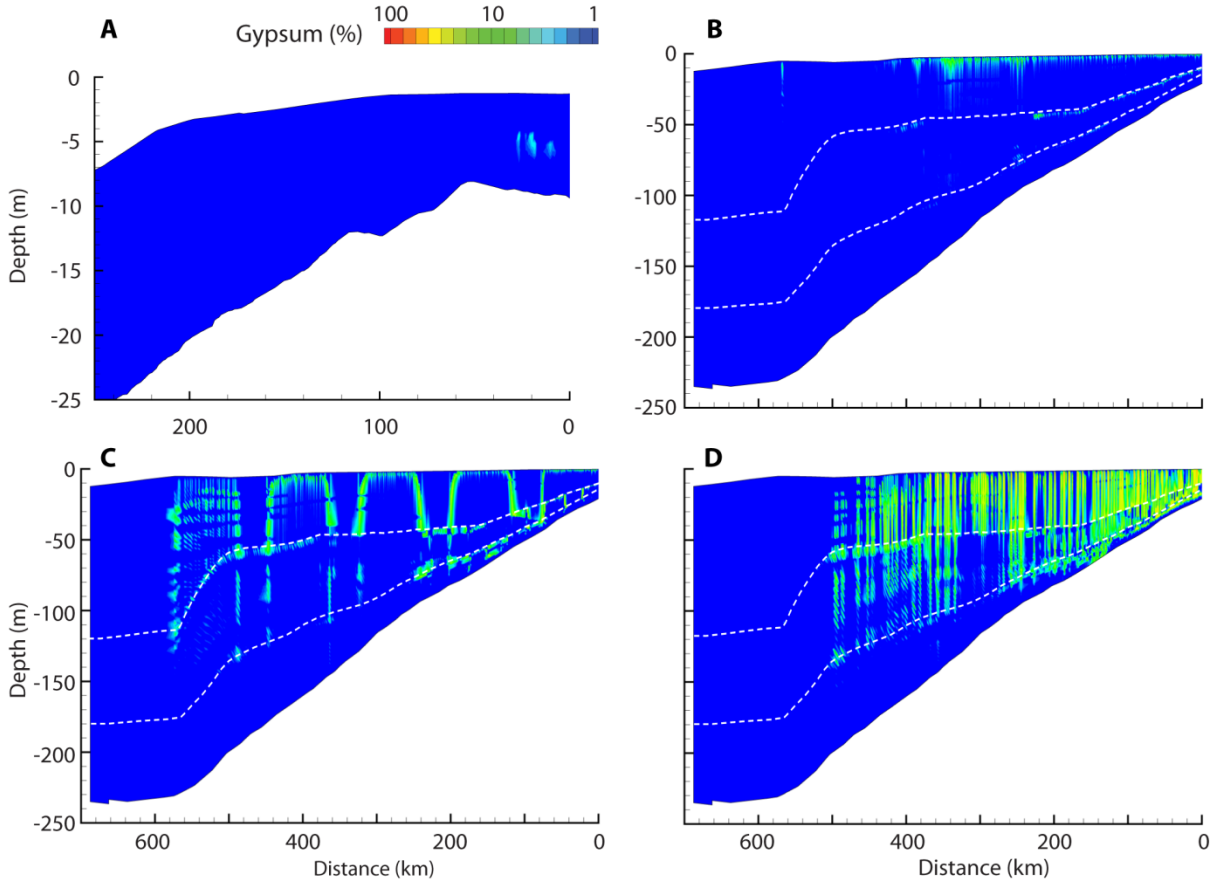
A
Gypsum (%)
100
10
1
Depth (m)
0
-5
-10
-15
-20
-25
200
100
0
B
0
-50
-100
-150
-200
-250
C
0
-50
-100
-150
-200
-250
600
400
200
0
Distance (km)
D
600
400
200
0
Distance (km)

Fig. A

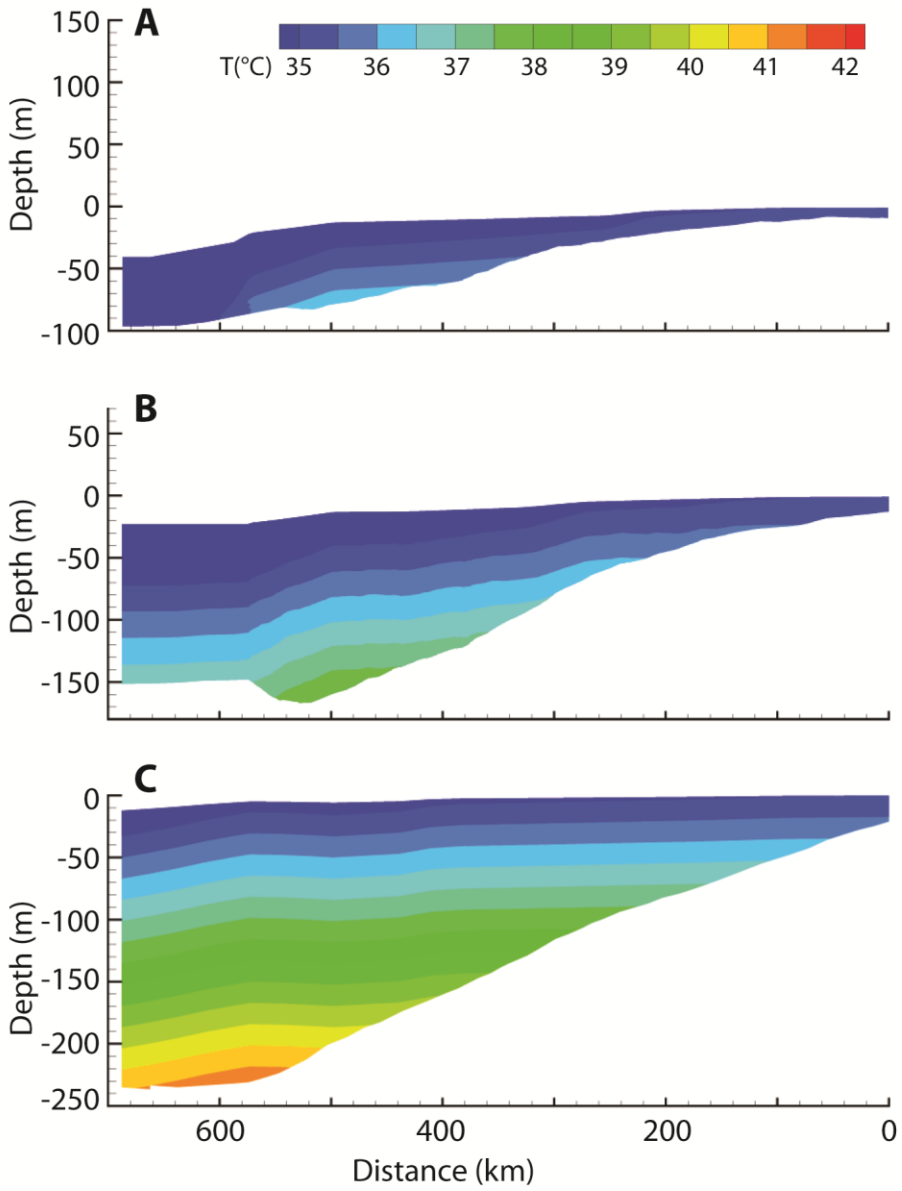
A
T(°C) 35 36 37 38 39 40 41 42
150
100
50
0
-50
-100
Depth (m)
B
50
0
-50
-100
-150
Depth (m)
C
0
-50
-100
-150
-200
-250
Depth (m)
600
400
200
0
Distance (km)

Fig. B

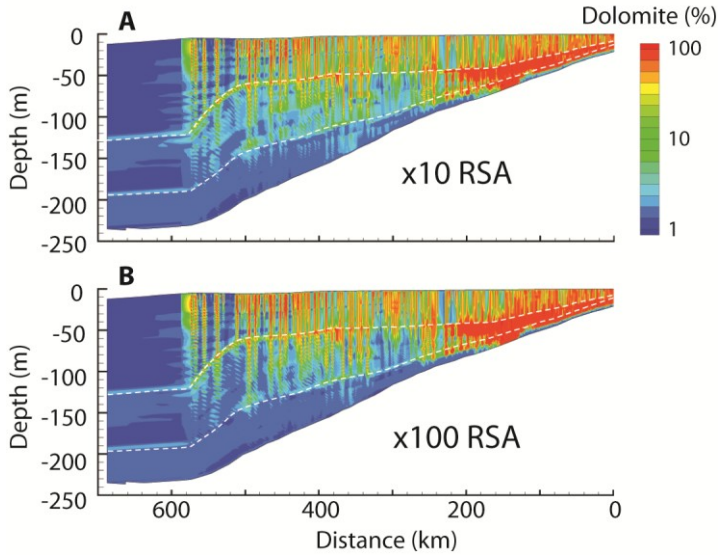
A
B
Dolomite (%)
100
10
1
Depth (m)
0
-50
-100
-150
-200
-250
x10 RSA
x100 RSA
600
400
200
0
Distance (km)

Fig. C

Table 1: Rock properties.

[a] Rock type	Texture	Fine fraction (F_f)	Initial porosity (%)	Horizontal permeability (m^2)	Anisotropy (Kh/Kv)	Reactive surface area (m^2/kg)
Outer ramp (OUT)	MS	0.95	81	7.94^{-14}	50	47.7
Middle ramp (MID)	WS	0.75	75	1.19^{-13}	5	38.7
Lower shoreface (LSF)	PS/GS	0.6	70	1.71^{-13}	50	32
Middle-upper shoreface (MUS)	PS/GS	0.15	46	9.19^{-13}	10	11.7
Restricted upper shoreface (RUS)	GS	0.05	45	8.49^{-12}	5	7.2
Backshoal-lagoonal (BSL)	micropeloidal GS	0.3	57	4.47^{-13}	5	18.5
Restricted lagoon (RL)	MS/WS	0.9	79	8.74^{-14}	2	45.5
Intertidal (IT)	MS	0.95	81	7.94^{-14}	50	47.7
Supratidal (ST)	MS	0.95	81	7.94^{-14}	100	47.7
Peritidal evaporites (PTE)	-	0.95	81	7.94^{-14}	500	47.7

[a] Rock types were derived from the 16 facies described by Sonnenfeld (1996b) by merging those with similar texture: laminated limestone/argillite couplets and bioturbated limestones/argillite couplets were coupled into the Outer ramp, ostracod-peloid dolomudstone/wackestone, chondrites dolomudstone and wave rippled dolomudstone/wackestone into the Restricted lagoon, and stromatolitic laminated mudstone/bindstone, laminated argillaceous dolomudstone and dolomudstone-rich evaporite solution collapse breccia into the Supratidal.

Table 2: Summary of key features of simulations.

Simulation number	Model dimension	Scale	Thermal regime	Rate of injection (m/yr)	Sequences	Number of brine pools	Figure
1	1D	inter-well	isothermal	0.001-1	I	1	7
2	2D	inter-well	isothermal	0.001-0.01	I	1	8
3	2D	regional	isothermal	0.001	I	1	9A-C,E,G; 10
4	2D	regional	non-isothermal	density driven	I-II-III	1	9A, B, D, F, H; 11
5	2D	regional	non-isothermal	density driven	I-II-III	5	12A-E
6	2D	regional	non-isothermal	density driven	I-II-III	1 with random brine salinity	12A,E-H; 13